Monthly Notices
of the
ROYAL ASTRONOMICAL SOCIETY

Mon. Not. R. Astron. Soc. **420,** 2064–2086 (2012) doi:10.1111/j.1365-2966.2011.20165.x

Constraining the absolute orientation of η Carinae's binary orbit: a 3D dynamical model for the broad [Fe III] emission⋆

T. I. Madura,[1]† T. R. Gull,[2] S. P. Owocki,[3] J. H. Groh,[1] A. T. Okazaki[4] and C. M. P. Russell[3]

[1]*Max-Planck-Institut für Radioastronomie, Auf dem Hügel 69, D-53121 Bonn, Germany*
[2]*Astrophysics Science Division, Code 667, NASA Goddard Space Flight Center, Greenbelt, MD 20771, USA*
[3]*Bartol Research Institute, Department of Physics and Astronomy, University of Delaware, Newark, DE 19716, USA*
[4]*Faculty of Engineering, Hokkai-Gakuen University, Toyohira-ku, Sapporo 062-8605, Japan*

Accepted 2011 November 8. Received 2011 November 7; in original form 2011 September 29

ABSTRACT

We present a three-dimensional (3D) dynamical model for the broad [Fe III] emission observed in η Carinae using the *Hubble Space Telescope*/Space Telescope Imaging Spectrograph (STIS). This model is based on full 3D smoothed particle hydrodynamics simulations of η Car's binary colliding winds. Radiative transfer codes are used to generate synthetic spectroimages of [Fe III] emission-line structures at various observed orbital phases and STIS slit position angles (PAs). Through a parameter study that varies the orbital inclination i, the PA θ that the orbital plane projection of the line of sight makes with the apastron side of the semimajor axis and the PA on the sky of the orbital axis, we are able, for the first time, to tightly constrain the absolute 3D orientation of the binary orbit. To simultaneously reproduce the blueshifted emission arcs observed at orbital phase 0.976, STIS slit PA $= +38^\circ$ and the temporal variations in emission seen at negative slit PAs, the binary needs to have an $i \approx 130^\circ$ to 145°, $\theta \approx -15^\circ$ to $+30^\circ$ and an orbital axis projected on the sky at a PA $\approx 302^\circ$ to 327° east of north. This represents a system with an orbital axis that is closely aligned with the inferred polar axis of the Homunculus nebula, in 3D. The companion star, η_B, thus orbits clockwise on the sky and is on the observer's side of the system at apastron. This orientation has important implications for theories for the formation of the Homunculus and helps lay the groundwork for orbital modelling to determine the stellar masses.

Key words: hydrodynamics – line: formation – binaries: close – stars: individual: Eta Carinae – stars: mass-loss – stars: winds, outflows.

1 INTRODUCTION

η Carinae is the most luminous, evolved stellar object that can be closely studied (Davidson & Humphreys 1997). Its immense luminosity ($L \gtrsim 5 \times 10^6\,L_\odot$; Cox et al. 1995) and relative proximity ($D = 2.3 \pm 0.1$ kpc; Smith 2006) make it possible to test and constrain specific theoretical models of extremely massive stars ($\gtrsim$60 $M_\odot$) using high-quality data (Hillier et al. 2001, 2006; Smith & Owocki 2006). η Car is thus one of the most intensely observed stellar systems in the Galaxy, having been the focus of numerous ground- and space-based observing campaigns at multiple wavelengths from radio (Duncan & White 2003; White et al. 2005) to gamma-rays (Tavani et al. 2009; Abdo et al. 2010).

Unfortunately, the dusty Homunculus nebula that formed during η Car's 'Great Eruption' in the 1840s enshrouds the system, complicating direct observations of the central stellar source (Smith 2009). Nevertheless, ground- and space-based, multiwavelength observations obtained over the past two decades strongly indicate that η Car is a highly eccentric ($e \sim 0.9$) colliding wind binary (CWB) with a 5.54-yr orbital period (Damineli 1996; Feast, Whitelock & Marang 2001; Duncan & White 2003; Smith et al. 2004; Whitelock et al. 2004; Corcoran 2005, 2011, hereafter C11; Verner, Bruhweiler & Gull 2005; van Genderen et al. 2006; Damineli et al. 2008a,b; Fernández-Lajús et al. 2010). The consensus view is that the primary star, η_A, is a luminous blue variable (LBV; Hillier & Allen

⋆Based on observations made with the NASA/ESA *Hubble Space Telescope*. Support for programs 7302, 8036, 8483, 8619, 9083, 9337, 9420, 9973, 10957 and 11273 was provided by NASA directly to the STIS Science Team and through grants from the Space Telescope Science Institute, which is operated by the Association of Universities for Research in Astronomy, Inc., under NASA contract NAS 5-26555.

†E-mail: tmadura@mpifr-bonn.mpg.de

1992; Davidson & Humphreys 1997; Hillier et al. 2001, 2006). Radiative transfer modelling of *Hubble Space Telescope*/Space Telescope Imaging Spectrograph (*HST*/STIS) spatially resolved spectroscopic observations suggests that η_A has a current mass $\gtrsim$90 $M_\odot$, and a current-day stellar wind with a mass-loss rate of $\sim 10^{-3}\,M_\odot\,yr^{-1}$ and terminal speed of ∼500–600 km s^{-1} (Hillier et al. 2001, 2006, hereafter H01, H06). The companion star, η_B, continues to evade direct detection since η_A dwarfs its emission at most wavelengths (Damineli et al. 2000; H01, H06; Smith et al. 2004; C11). As a result, η_B's stellar parameters, evolutionary state, orbit and influence on the evolution of η_A are poorly known.

Currently, the best constraints on the stellar properties of η_B come from photoionization modelling of the 'Weigelt blobs', dense, slow-moving ejecta in the vicinity of the binary system (Weigelt & Ebersberger 1986). Verner et al. (2005) initially characterized η_B as a mid-O to WN supergiant. More recent work by Mehner et al. (2010) tightly constrains the effective temperature of η_B ($T_{\rm eff}$ ∼ 37 000–43 000 K), but not its luminosity ($\log L/L_\odot \sim 5$ to 6), resulting in a larger range of allowed stellar parameters.

Constraints on the wind parameters of η_B come from extended X-ray monitoring by the *Rossi X-ray Timing Explorer* (*RXTE*), *Chandra*, *XMM* and *Suzaku* satellites (Ishibashi et al. 1999; Corcoran 2005; Hamaguchi et al. 2007; Corcoran et al. 2010). The periodic nature, minimum around periastron and hardness (up to 10 keV) of η Car's *RXTE* light curve are all characteristics of a highly eccentric CWB, the variable X-ray emission arising in a wind–wind collision (WWC) zone formed between the two stars (Pittard & Corcoran 2002; Okazaki et al. 2008; Parkin et al. 2009, 2011; Corcoran et al. 2010, hereafter PC02, O08, P09, P11 and C10, respectively). The hardness of the X-rays requires that η_B have a high wind terminal speed of ∼3000 km s^{-1}, and detailed modelling of the momentum balance between the two shock fronts suggests a mass-loss rate of $\sim 10^{-5}\,M_\odot\,yr^{-1}$ (PC02; O08; P09, P11).

Proper numerical modelling of η Car's WWC remains a challenge, mainly because it requires a full three-dimensional (3D) treatment since orbital motion, especially during periastron, can be important or even dominant, affecting the shape and dynamics of the WWC region (O08; P09, P11). Most hydrodynamical simulations of η Car have been two-dimensional (2D), neglecting the effects of orbital motion for simplicity (Pittard 1998, 2000; PC02; Henley 2005). Until very recently (O08; P11), fully 3D simulations were computationally impractical.

When it comes to reproducing observational diagnostics of η Car from hydrodynamical simulations of its colliding winds, the focus has been almost exclusively on X-rays. One drawback of this is that models for η Car at other wavelengths have been mostly phenomenological, offering only qualitative explanations for the vast array of complicated observations. This makes it difficult to test and refine models, or quantitatively constrain the physical parameters of the system. An excellent example is the lack of consensus regarding η Car's orbital orientation. The majority favour an orbit in which η_B is behind η_A during periastron (Damineli 1996; PC02; Corcoran 2005; Hamaguchi et al. 2007; Nielsen et al. 2007a; Damineli et al. 2008b; Henley et al. 2008; O08; P09, P11; Groh et al. 2010b; Richardson et al. 2010). But others place η_B on the near side of η_A at periastron (Abraham et al. 2005; Falceta-Gonçalves, Jatenco-Pereira & Abraham 2005; Abraham & Falceta-Gonçalves 2007; Kashi & Soker 2007, 2008; Falceta-Gonçalves & Abraham 2009). Some claim that the orientation is not well established at all (Mehner et al. 2011).

A more fundamental drawback of focusing purely on X-rays or other spatially unresolved data is that any derived orbit is ambiguous with respect to its *absolute* orientation on the sky; *any orbital orientation derived solely from fitting the X-ray data can be rotated on the sky about the observer's line of sight and still match the observations*. A degeneracy also exists in the orbital inclination, with models that assume $i \approx 45^\circ$ and $\approx 135^\circ$ both capable of fitting the observed *RXTE* light curve. However, high-resolution spatial information is not enough; moderate-resolution spectral data is needed to determine the velocity structure of the emitting gas, and thus fully constrain the orbital orientation. As a result, using X-ray data alone, it is impossible to determine the 3D alignment or misalignment of the orbital axis with the Homunculus polar axis, or the direction of the orbit. It is commonly *assumed* that the orbital axis is aligned with the Homunculus polar axis, but to date, neither modelling nor observations have unambiguously demonstrated that this is the case. Knowing the orbit's orientation is key to constraining theories for the cause of the Great Eruption and formation of the Homunculus (i.e. single star versus binary interaction/merger scenarios; Iben 1999; Dwarkadas & Owocki 2002; Smith et al. 2003; Soker 2007; Smith 2009, 2011; Smith & Frew 2011). Furthermore, a precise set of orbital parameters would lay the groundwork for orbital modelling to determine the stellar masses.

In a recent attempt to characterize η Car's interacting winds, Gull et al. (2009, hereafter G09) presented an analysis of *HST*/STIS observations taken between 1998 and 2004, identifying spatially extended (up to 0.8 arcsec), velocity-resolved forbidden emission lines from low- and high-ionization[1] species. *HST*/STIS imaging spectroscopy is ideal for moving beyond X-ray signatures as it uniquely provides the spatial (∼0.1 arcsec) *and* spectral ($R \sim 8000$) resolution necessary to separate the spectra of η Car's central source and nearby circumstellar ejecta from those of the Homunculus and other surrounding material. Moreover, this high-ionization forbidden emission is phase locked, which strongly suggests it is regulated by the orbital motion of η_B. Observed spectroimages are also highly dependent on the position angle (PA)[2] of the *HST*/STIS slit, implying that they contain valuable geometrical information. This opens up the possibility of obtaining η_B's orbital, stellar and wind parameters through proper modelling of the extended forbidden line emission.

This paper presents a detailed 3D dynamical model for the broad components of the high-ionization forbidden line emission observed in η Car using the *HST*/STIS. Our model is based on the results of full 3D smoothed particle hydrodynamics (SPH) simulations of η Car's colliding winds (Sections 3.2 and 4.1). Radiative transfer calculations performed with a modified version of the SPLASH code (Price 2007) are used with IDL routines to generate synthetic spectroimages of [Fe III] emission-line structures at various orbital phases and STIS slit PAs (Section 3.4). Through a parameter study that varies the orbital inclination, the angle that the line of sight makes with the apastron side of the semimajor axis, and the PA on the sky of the projected orbital axis, we are able to tightly constrain, for the first time, the *absolute* (3D) orientation and direction of η Car's orbit (Section 4), showing in particular that the orbital axis is closely aligned in 3D with the inferred polar axis of the Homunculus nebula. A discussion of the results and this derived orientation are in Section 5. Section 6 summarizes our conclusions and outlines the direction of future work. We begin (Section 2) with a brief summary of the observations used in this paper.

[1] Low- and high-ionization refer here to atomic species with ionizations potentials (IPs) below and above the IP of hydrogen, 13.6 eV.
[2] Measured in degrees from north to east.

2 THE OBSERVATIONS

This paper uses the same *HST*/STIS data described in G09 (see their table 1). Extracted portions of observations recorded from 1998 March to 2004 March with the STIS CCD (0.0507 arcsec pixel^{-1} scale) with medium dispersion gratings ($R \sim 8000$), in combination with the 52×0.1 arcsec^2 slit from 1640 to 10 100 Å, were used to sample the spectrum of the central core of η Car. Phases of the observations, ϕ, are relative to the *RXTE* X-ray minimum at 1997.9604 (Corcoran 2005): $\mathrm{JD_{obs}} = \mathrm{JD}\,245\,0799.792 + 2024.0 \times \phi$. Solar panel orientation requirements constrained the STIS slit PAs. The reduced STIS CCD spectra available through the STScI archives (http://archive. stsci.edu/prepds/etacar/) were used. Compass directions (NW = north-west, etc.) describe the spatial extent of the emission. All wavelengths are in vacuum and velocities are heliocentric. For details, see G09 and references therein.

Fig. 1 shows examples of resolved, broad emission from [Fe III] λ4659. In the top centre panel, faint spatially- and velocity-resolved emission can be seen against bright nebular emission and dust-scattered stellar radiation. Strong, narrow-line emission from the SW of η Car is also seen. The bright continuum close to the wavelength of the wind line of interest is subtracted on a spatial row-by-row basis in order to isolate the fainter broad forbidden line emission (top right-hand panel of Fig. 1). All spectroimages in this paper have been processed identically using a portion of the spectrum with no bright narrow- or broad-line contamination. Row-by-row subtraction across the stellar position is less successful due to insufficient correction in the data reduction for small tilts of the spectrum on the CCD (G09).

The bottom right-hand panel of Fig. 1 contains the same spectroimage of [Fe III] λ4659 as the top right-hand panel, but with masks that remove narrow line contamination from the Weigelt blobs, and contamination to the red due to the nearby [Fe II] λ4666 wind line. The masks are intended to remove 'distracting' emission features not relevant to the work in this paper, displaying only the observed broad structures that are the focus of the modelling (outlined in white). To determine the spatial and spectral ranges where [Fe II] λ4666 contaminates the [Fe III] λ4659 image, we use as a template the uncontaminated spectroimage of the bright [Fe II] λ4815 line (bottom centre panel of Fig. 1). We also compare the [Fe III] λ4659 images to those of the [Fe III] λ4702 and [N II] λ5756 lines, which form in nearly identical conditions as they have very similar critical densities and IPs (table 3 of G09). A detailed discussion of the observations and masking procedure for all spectroimages modelled in this paper is in Appendix A (available in the online version of this paper – see Supporting Information).

2.1 The key observational constraints modelled

Three key features observed in spectroimages of the high-ionization forbidden line emission can be used to constrain the 3D orientation of η Car's orbit. Each provides important clues about the nature and orbital variation of η Car's interacting winds. We briefly summarize these below.

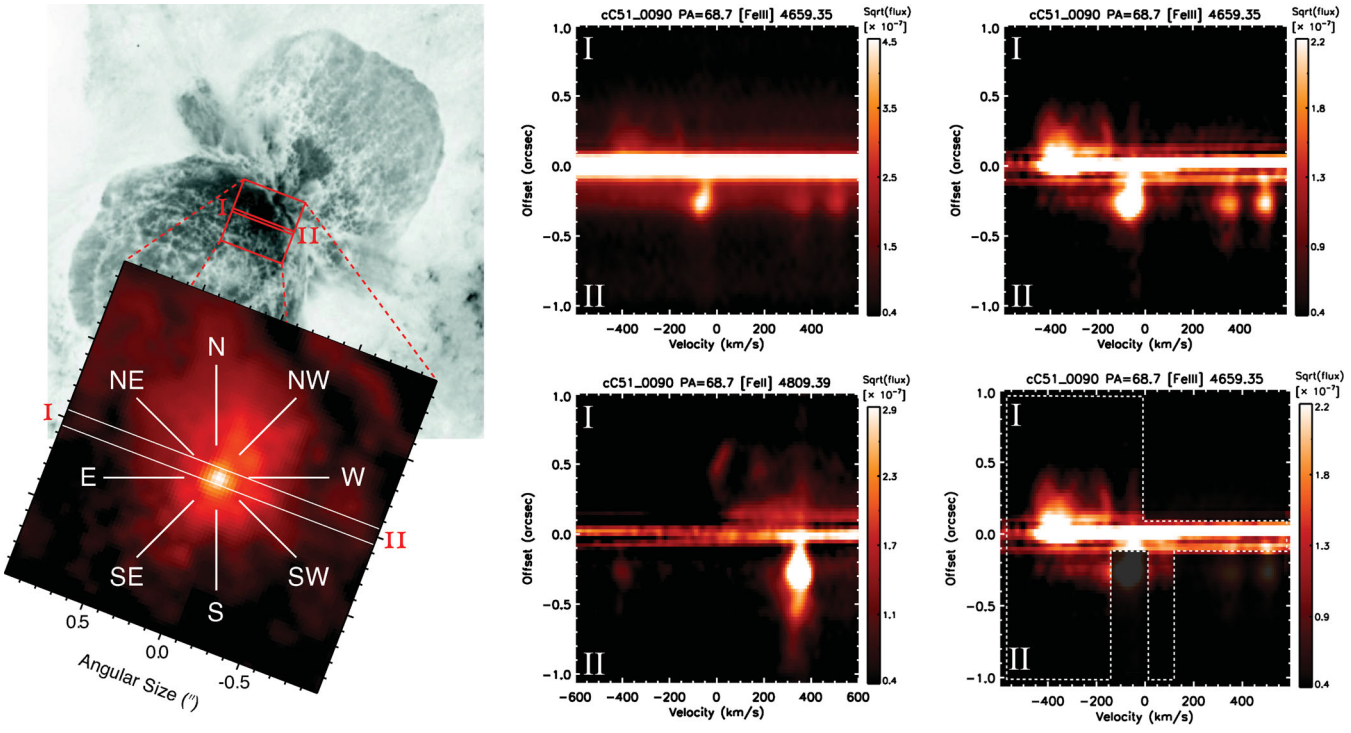

Figure 1. Examples of the *HST*/STIS spatially resolved [Fe III] spectra. Top left: an *HST*/Advanced Camera for Surveys (ACS) High Resolution Camera (HRC) image of the Homunculus and η Car with a 20 arcsec field of view. Bottom left: enlarged central 2 arcsec field of view with the 52×0.1 arcsec^2 slit positioned at PA $= +69^\circ$ and directional labels (NW) included for reference in the text. Spectroimages in the middle and right-hand columns were recorded from the central 2×0.1 arcsec^2 portion of the slit, as drawn between labels I and II. Top centre: spatially resolved line profile of [Fe III] λ4659 in original form, recorded at PA $= +69^\circ$ in 2002 July ($\phi = 0.82$). Top right: the same spectroimage with the continuum subtracted on a spatial row-by-row basis. The velocity scale, referenced to the vacuum rest wavelength of the line, is ± 600 km s^{-1}, and the colour level is proportional to the square root of the intensity. Bottom centre: spectroimage of [Fe II] λ4815, shifted by 400 km s^{-1}, used as a template to determine the spatial and spectral ranges where the [Fe III] image is contaminated by [Fe II] λ4666 emission. Bottom right: same spectroimage as the top right-hand panel, but with masks that remove the narrow line contamination and the contamination to the red from nearby [Fe II] λ4666 (see text).

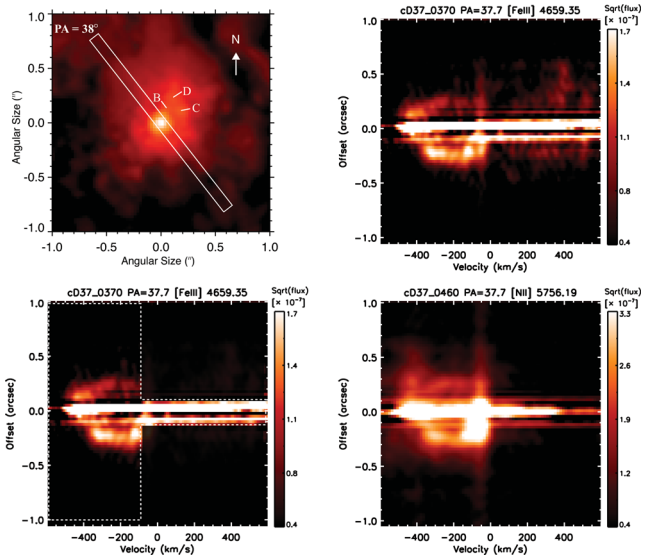

Figure 2. Spectroimages recorded 2003 May 5 ($\phi = 0.976$). Top left-hand panel: *HST*/ACS HRC image of the central 2 arcsec of η Car with the 2 arcsec long portion of the STIS slit at PA = +38° overlaid. The locations of Weigelt blobs B, C and D are indicated, as is the direction of north. Top right-hand panel: continuum-subtracted spectroimage of [Fe III] λ4659. Emission appears as a pair of completely blueshifted arcs. Colour is proportional to the square root of the intensity and the velocity scale is $\pm 600\,\mathrm{km\,s^{-1}}$. Weak emission to the red is entirely due to contamination by [Fe II] λ4666, while weak, narrow emission is centred at $\sim -40\,\mathrm{km\,s^{-1}}$. Bottom left-hand panel: same spectroimage, but with masks that remove the line contamination. Bottom right-hand panel: continuum-subtracted spectroimage of [N II] λ5756 included to demonstrate that at this phase and STIS PA, the high-ionization forbidden lines show no evidence of broad, spatially extended, redshifted emission.

2.1.1 Constraint 1: emission arcs at slit PA = +38°, φ = 0.976

Fig. 2 displays observed spectroimages of [Fe III] λ4659, recorded at slit PA = +38° on 2003 May 5 ($\phi = 0.976$), showing spatially extended (up to ∼0.35 arcsec) emission in the form of very distinct, nearly complete arcs that are entirely blueshifted, up to $\sim -475\,\mathrm{km\,s^{-1}}$. Several weaker [Fe III] lines nearby in the spectrum, while blended, show no evidence of a spatially extended (>0.1 arcsec) red component, and no other high-ionization forbidden lines show an extended red component at this position (G09). To illustrate this, the bottom right-hand panel of Fig. 2 contains a continuum-subtracted spectroimage of [N II] λ5756, taken at the same orbital phase and slit PA. The IP (14.5 eV) and critical density ($3 \times 10^7\,\mathrm{cm^{-3}}$) of [N II] λ5756 are very similar to that of [Fe III] λ4659 (16.2 eV and $\sim 10^7\,\mathrm{cm^{-3}}$), meaning that their spatially extended emission forms in nearly identical regions and via the same physical mechanism. The [N II] λ5756 line is strong and located in a spectral region with very few other lines. Unlike [Fe III] λ4659, there is no contamination to the red of [N II] λ5756, making it ideal for demonstrating that there is no spatially extended, redshifted, broad high-ionization forbidden line emission.

Of particular importance are the asymmetric shape and intensity of these emission arcs. Both arcs extend to nearly the same spatial distance from the central core, but the upper arc is noticeably dimmer and stretches farther to the blue, to $\sim -475\,\mathrm{km\,s^{-1}}$. The lower arc is brighter, but only extends to $\sim -400\,\mathrm{km\,s^{-1}}$. Every high-ionization forbidden line observed at this orbital phase and slit PA exhibits these asymmetries in intensity and velocity (figs 6–9 of G09), indicating that they are independent of the IP and critical density of the line and intrinsic to the shape and distribution of the photoionized extended wind material in which the lines form. As such, the shape and asymmetry of the blueshifted emission arcs may be used to help constrain the orbital orientation.

2.1.2 Constraint 2: variations with orbital phase at constant slit PA = −28°

Let us focus next on shifts of the high-ionization forbidden emission with orbital phase. Fig. 11 of G09 shows sets of six spectra of [Fe III] λ4659 and λ4702 recorded at select phases at slit PA = −28°. During the two minima at $\phi = 0.045$ and 1.040 (rows 1 and 5 of fig. 11 of G09), the broad [Fe III] emission is absent. By $\phi = 0.213$ (row 2) and $\phi = 1.122$ (row 6, ∼8 months after the X-ray minimum), it strongly reappears. Images at $\phi = 0.407$ are similar to those at $\phi = 0.213$ and 1.122. By $\phi = 0.952$, emission above $\sim 150\,\mathrm{km\,s^{-1}}$ disappears. This phase dependence in the [Fe III] emission, especially the disappearance during periastron, strongly indicates that it is tied to the orbital motion of η_B.

Another important observational feature is the presence of spatially extended *redshifted* emission to the NW, in addition to extended blueshifted emission to the SE, at phases far from periastron. This is in contrast to the entirely blueshifted arcs seen for slit PA = +38°, indicating that the STIS slit at PA = −28° is sampling different emitting portions of η Car's extended wind structures, even at similar orbital phases.

2.1.3 Constraint 3: Doppler shift correlations with orbital phase and slit PA

The final set of observations focuses on changes with slit PA leading up to periastron. Figs 12 and 13 of G09 illustrate the behaviour of the [Fe III] emission for various slit PAs at select phases. The key point to take away from this particular data set is that away from periastron, the spatially extended [Fe III] emission is almost entirely blueshifted for positive slit PAs = +22° to +70°, but is partially redshifted for negative PAs, most notably PA = −82°.

3 A 3D DYNAMICAL MODEL FOR THE BROAD HIGH-IONIZATION FORBIDDEN LINE EMISSION

3.1 Why model [Fe III] λ4659 emission?

Table 3 of G09 lists the various forbidden emission lines observed in η Car. However, there are several important reasons to focus particular attention on [Fe III] λ4659 emission.

First, the physical mechanism for the formation of forbidden lines is well understood (Appendix B, available in the online version of this paper – see Supporting Information). Moreover, emission from forbidden lines is optically thin. Thus, forbidden line radiation can escape from a nebula much more easily than radiation from an optically thick resonance line, which is emitted and reabsorbed many times (Hartman 2003). This is of great value when studying an object so enshrouded by circumstellar material since one does not have to model complicated radiative transfer effects.

[Fe III] is considered rather than a lower ionization line of [Fe II] because *the bulk of the* [Fe III] *emission arises in regions that are directly photoionized by* η_B (Verner et al. 2005; G09; Mehner et al. 2010). No intrinsic [Fe III] emission is expected from η_A. This is

based on detailed theoretical models by H01 and H06, which show that in η_A's envelope, Fe^{2+} only exists in regions where the electron density is two-to-four orders of magnitude higher than the critical density of the [Fe III] λ4659 line. Since Fe^0 needs 16.2 eV radiation (or collisions) to reach the Fe^{2+} state, most of the [Fe III] emission arises in areas directly photoionized by η_B.

In comparison, Fe^0 only needs 7.9 eV radiation or collisions to ionize to Fe^+, which can form in the wind of η_A (without η_B's influence) and/or near the wind–wind interaction regions in areas excited by mid-UV radiation filtered by η_A's dense wind. Collisions and photoexcitation to upper Fe^+ energy levels can also populate many metastable levels. As a result, [Fe II] emission is far more complicated and originates from lower excitation, lower density regions on much larger spatial scales (H01, H06; G09; Mehner et al. 2010). Because of this complexity, the modelling of [Fe II] emission is deferred to future work.

The IP of 16.2 eV required for Fe^{2+} also means that the [Fe III] emission forms in regions where hydrogen is ionized, but helium is still neutral. In contrast, both Ar^{2+} and Ne^{2+} have IPs greater than 24.6 eV. Therefore, [Ar III] and [Ne III] emission arise in areas where helium is singly ionized. Modelling [Fe III] is thus more straightforward as one does not have to worry about the two different types of ionization structure possible (one due to H and one due to He), which depend on the spectrum of ionizing radiation and the abundance of helium (Osterbrock 1989).

[Fe III] λ4659 is chosen over the similar emission line of [N II] λ5756 in order to avoid potential complications due to intrinsic [N II] emission in the extended wind of η_A. [N II] emission can form in a broad zone between 100 and $1000R_*$ (∼30–300 au) of η_A and is sensitive to its wind temperature and mass-loss rate (H01). By focusing on [Fe III], one avoids having to include any intrinsic forbidden line emission from η_A.

The modelling in this paper focuses solely on the *broad* [Fe III] emission features that are thought to arise in the dense, moderate velocity (∼100–600 km s^{-1}) extended primary wind and WWC regions. The much narrower ($\lesssim$50 km s^{-1}) emission features that form in the Weigelt blobs and other dense, slow-moving equatorial ejecta from η Car's smaller eruption in the 1890s (Weigelt & Ebersberger 1986; Davidson et al. 1995, 1997; Ishibashi et al. 2003; Smith et al. 2004; G09; Mehner et al. 2010) are not modelled. Any possible effects of local dust formation are neglected for simplicity as not enough information is available to realistically include them at this time (Williams 2008; Mehner et al. 2010).

As all observed high-ionization forbidden lines show the same basic spatial and temporal features in their broad emission, with any differences in size or location attributable to differences in the IP and critical density of the specific line of interest, focusing solely on [Fe III] λ4659 should not significantly bias the overall conclusions, which should extend to the other high-ionization forbidden lines as well. Values of the transition probability ($A_{21} = 0.44$ s^{-1}), statistical weights ($g_1 = g_2 = 9$) and line transition frequency ($\nu_{21} = 6.435 \times 10^{14}$ s^{-1}) for [Fe III] λ4659 all come from Nahar & Pradhan (1996). Values for the collision strengths (Ω_{12}) come from Zhang (1996). A solar abundance of iron is also used, consistent with the works of H01, H06 and Verner et al. (2005).

3.2 The 3D SPH code and general problem set-up

The numerical simulations in this paper were performed with the same 3D SPH code used in O08. The stellar winds are modelled by an ensemble of gas particles that are continuously ejected with a given outward velocity at a radius just outside each star. For simplicity, both winds are taken to be adiabatic, with the same initial temperature (35 000 K) at the stellar surfaces and coasting without any net external forces, assuming that gravitational forces are effectively cancelled by radiative driving terms (O08). The gas has negligible self-gravity and adiabatic cooling is included.

Table 1. Stellar, wind and orbital parameters of the 3D SPH simulation.

Parameter	η_A	η_B
Mass ($M_\odot$)	90	30
Radius ($R_\odot$)	90	30
Mass-loss rate ($M_\odot$ yr^{-1})	10^{-3}	10^{-5}
Wind terminal velocity (km s^{-1})	500	3000
Orbital period (d)	2024	
Orbital eccentricity e	0.9	
Semimajor axis length a (au)	15.4	

In a standard *xyz* Cartesian coordinate system, the binary orbit is set in the *xy* plane, with the origin at the system centre-of-mass and the orbital major axis along the *x*-axis. The two stars orbit counter-clockwise when looking down on the orbital plane along the $+z$ axis. Simulations are started with the stars at apastron and run for multiple consecutive orbits. By convention, $t = 0$ ($\phi = 0$) is defined to be at periastron passage.

To match the ∼±0.7 arcsec scale of the STIS observations at the adopted distance of 2.3 kpc to the η Car system (Smith 2006), the outer simulation boundary is set at $r = \pm 105a$ from the system centre-of-mass, where a is the length of the orbital semimajor axis ($a = 15.4$ au). Particles crossing this boundary are removed from the simulation. We note that the SPH formalism is ideally suited for such large-scale 3D simulations, as compared to grid-based hydrodynamics codes (Price 2004; Monaghan 2005).

Table 1 summarizes the stellar, wind and orbital parameters used in the modelling, which are consistent with those derived from the observations (H01, H06; PC02; C11), with the exception of the wind temperature of η_A. The effect of the wind temperature on the dynamics of the high-velocity wind collision is negligible (O08). Note that the simulation adopts the higher mass-loss rate for η_A derived by Davidson et al. (1995), Cox et al. (1995), H01 and H06, rather than the factor of four lower mass-loss rate assumed when analysing X-ray signatures (PC02; O08; P09, P11; C11). Effects of the adopted value of the primary mass-loss rate on the forbidden line emission will be the subject of a future paper.

The publicly available software SPLASH (Price 2007) is used to visualize the 3D SPH code output. SPLASH differs from other tools because it is designed to visualize SPH data using SPH algorithms. There are a number of benefits to using SPLASH, and the reader is referred to Price (2007) and the SPLASH user guide for these and discussions on the interpolation algorithms.

3.3 Generation of synthetic slit spectroimages

The 3D SPH simulation provides the time-dependent, 3D density and temperature structure of η Car's interacting winds on spatial scales comparable to those of the *HST*/STIS observations. This forms the basis of our 3D dynamical model. Unfortunately, it is currently not possible to perform full 3D simulations of η Car in which the radiative transfer is properly coupled to the hydrodynamics (Paardekooper 2010). Instead, the radiative transfer calculations here are performed as post-processing on the 3D SPH simulation

output. This should not strongly affect the results so long as the material that is photoionized by η_B responds nearly instantaneously to its UV flux. In other words, as long as the time-scale for the recombination of $e + Fe^{2+} \rightarrow Fe^{+}$ is very small relative to the orbital time-scale, the calculations should be valid.

The recombination time-scale is $\tau_{rec} = 1/(\alpha_{rec} n_e)$ s, where $\alpha_{rec}(T)$ is the recombination rate coefficient (in units of $cm^3\ s^{-1}$) at temperature T and n_e is the electron number density. For $T \sim 10^4$ K, $\alpha_{rec}(T) \approx 4 \times 10^{-12}\ cm^3\ s^{-1}$ (Nahar 1997). Since densities near the critical density of the line are the primary focus, $n_e \sim 10^7\ cm^{-3}$; this gives $\tau_{rec} \approx 7$ h, which is much smaller than the orbital time-scale, even during periastron passage, which takes approximately one month. Any possible time-delay effects should not strongly affect the results as the light-travel-time to material at distances of ∼0.5 arcsec in η Car is only about one week.

3.3.1 *Summary of the basic procedure*

Synthetic slit spectroimages are generated using a combination of Interactive Data Language (IDL) routines and radiative transfer calculations performed with a modified version of the SPLASH (Price 2007) code. Here, we outline the basic procedure, with the specifics discussed in the following subsections.

Nearly all of the required calculations are performed within SPLASH, which reads in the 3D SPH code output for a specific orbital phase, rotates the data to a desired orbital orientation on the sky, and computes the line-of-sight velocity for all of the material. Next is the computation of the ionization volume created by η_B where Fe^+ is photoionized to Fe^{2+}. It is assumed that any material within this volume is in collisional ionization equilibrium, and that no material with $T > 250\,000$ K emits. All other material in the photoionization volume has its forbidden line emissivity calculated using equation (13), derived below. Material located outside the photoionization volume does not emit.

The intensity I is computed by performing a line-of-sight integration of the emissivity at each pixel, resulting in an image of the spatial distribution of the [Fe III] intensity projected on the sky. This is done for each velocity v_{bin} used along the dispersion axis of the synthetic slit in the velocity range of interest, resulting in a set of intensity images. The individual [Fe III] λ4659 intensity images are then combined and convolved with the *HST*/STIS response using IDL routines in order to create a synthetic position versus velocity spectroimage for comparison to the observations.

3.3.2 *Defining the binary orientation relative to the observer*

With the two stars orbiting in the xy plane, the 3D orientation of the binary relative to the observer is defined by the orbital inclination i, the prograde direction angle θ that the orbital plane projection of the observer's line of sight makes with the apastron side of the semimajor axis,[3] and the position angle *on the sky* of the $+z$ orbital axis, PA_z (Fig. 3).

Following the standard definition for binary systems, i is the angle that the line of sight makes with the $+z$-axis. An $i = 0°$ is a face-on orbit with the observer's line of sight along the $+z$-axis and the two stars orbiting counter-clockwise on the sky. An $i = 90°$ places the line of sight in the orbital xy plane, while $i = 180°$ is a face-on orbit with the two stars orbiting clockwise on the sky.

[3] θ is the same as the angle ϕ defined in fig. 3 of O08.

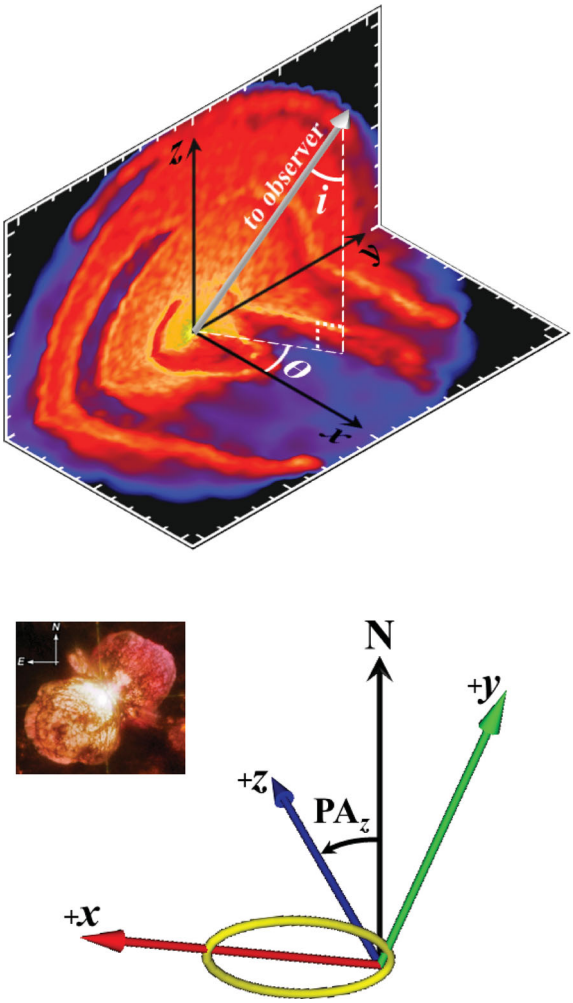

Figure 3. Diagrams illustrating the observer's position. Top: schematic defining the inclination angle i that the observer's line of sight makes with the $+z$ orbital axis, and the equatorial projection angle θ of the line of sight relative to the apastron side of the semimajor axis x. The background orthogonal planes show slices of density from the 3D SPH simulation at apastron in the xy orbital plane and the yz plane perpendicular to the orbital plane and major axis. Bottom: diagram defining the position angle on the sky, PA_z, of the $+z$ orbital axis (blue), measured in degrees counter-clockwise of north (N). The binary orbit projected on the sky is shown in yellow, as are the semimajor (red) and semiminor (green) axes. The small inset to the left is a *HST* WFPC2 image of the Homunculus (credit: NASA, ESA and the Hubble SM4 ERO Team) included for reference.

For $i = 90°$, a value of $\theta = 0°$ has the observer looking along the $+x$ axis (along the semimajor axis on the apastron side of the system), while a $\theta = 90°$ has the observer looking along the $+y$-axis. In the conventional notation of binary orbits, the 'argument of periapsis' $\omega = 270° - \theta$.

PA_z defines the position angle on the sky of the $+z$ orbital axis and is measured in degrees counter-clockwise of N. A $PA_z = 312°$ aligns the projected orbital axis with the Homunculus polar axis (Davidson et al. 2001; Smith 2006, 2009) and has $+z$ pointing NW on the sky. A $PA_z = 42°$ places the orbital axis perpendicular to the Homunculus polar axis with $+z$ pointing NE. A $PA_z = 132°$ (222°) is also aligned with (perpendicular to) the Homunculus polar axis and has $+z$ pointing SE (SW) on the sky.

3.3.3 *Volume of material photoionized by η_B*

Based on the models of η_A's envelope by H01 and H06, it is assumed that Fe^+ is initially the dominant ionization state of iron in primary wind material located $r > 50$ au from η_A, and that hydrogen and helium are initially neutral in the primary wind for distances of $r > 155$ and >3.7 au, respectively. The calculation of the volume of material photoionized from Fe^+ to Fe^{2+} by η_B follows that presented in Nussbaumer & Vogel (1987) for symbiotic star systems. For cases where hydrogen or helium alone determines the ionization structure, the boundary between neutral hydrogen (H^0) and ionized hydrogen (H^+) can be expressed analytically. As η_A's extended wind consists mostly of hydrogen and helium (fig. 9 of H01), and because the [Fe III] emission arises in regions where hydrogen is ionized but helium is not, such a calculation should provide a reasonable approximation for the size and shape of the photoionization boundary between Fe^+ and Fe^{2+}. This, however, is an upper limit for the photoionization volume since the IP of 16.2 eV required for Fe^{2+} is slightly larger than the 13.6 eV needed to ionize H^0.

In our calculation, the primary star is separated by a distance p from a hot companion star that emits spherically symmetrically L_H photons s^{-1} that are capable of ionizing H^0. The primary has a standard spherically symmetric mass-loss rate of $\dot{M}_1 = 4\pi r^2 \mu m_H n(r) v_\infty$, where $n(r)$ is the hydrogen number density, μ is the mean molecular weight, m_H is the mass of a hydrogen atom and v_∞ is the terminal speed of the primary wind.

In a small angle $\Delta\theta$ around the direction θ, the equilibrium condition for recombination-ionization balance is

$$L_H \frac{\Delta\theta}{4\pi} = \Delta\theta \int_0^{s_\theta} n(s) n_e(s) \alpha_B(H, T_e)\, s^2\, ds, \quad (1)$$

where s measures the distance from the ionizing secondary star in the direction θ, s_θ is the boundary between H^0 and H^+, α_B is the total hydrogenic recombination coefficient in case B at electron temperature T_e and n_e is the electron number density (Nussbaumer & Vogel 1987). The electron density can be written as

$$n_e(r) = (1 + a(\mathrm{He}))n(r), \quad (2)$$

where

$$n(r) = \frac{\dot{M}_1}{4\pi r^2 \mu m_H v_\infty}, \quad (3)$$

and a(He) is the abundance by number of He relative to H. Expressing both s and r in units of p, defining $u \equiv s/p$ and making the further approximation that α_B is constant (Nussbaumer & Vogel 1987), equation (1) can be written as

$$X^{H^+} = f(u, \theta), \quad (4)$$

where

$$X^{H^+} = \frac{4\pi\mu^2 m_H^2}{\alpha_B(1 + a(\mathrm{He}))} p L_H \left(\frac{v_\infty}{\dot{M}_1}\right)^2 \quad (5)$$

and

$$f(u, \theta) = \int_0^u \frac{x^2}{(x^2 - 2x\cos\theta + 1)^2}\, dx. \quad (6)$$

In the modified SPLASH routine, equation (4) is solved for a specified L_H. However, since equation (4) does not account for the effects of the WWC, we assume that mass is conserved and that all primary wind material normally within the cavity created by η_B is compressed into the walls of the WWC region, with the ionization state of the WWC zone walls before being photoionized the same as that of the primary wind (i.e. iron is in the Fe^+ state).

The stellar separation is computed directly from the 3D SPH simulation. We use the same value for the abundance by number of He to H as H01 and H06, a(He) = 0.2. A constant value of $\alpha_B = 2.56 \times 10^{-13}\,cm^3\,s^{-1}$ at $T_e = 10\,000$ K is also used (Osterbrock 1989). Based on Mehner et al. (2010) and Verner et al. (2005), the value of L_H is chosen to be that of an O5 giant with $T_{eff} \approx 40\,000$ K, which according to Martins, Schaerer & Hillier (2005) has a hydrogen ionizing flux of $10^{49.48}$ photons s^{-1}. Any shielding effects due to the presence of the Weigelt blobs or other dense, slow-moving equatorial ejecta are not presently included.

The third column of Fig. 6 illustrates the time variability of the photoionization region created by η_B for slices in the xy orbital plane. The region is largest around apastron, when η_B is farthest from η_A's dense wind. As η_B moves closer to η_A, the photoionization zone becomes smaller and more wedge shaped[4] due to the gradual embedding of η_B in η_A's wind. During periastron, η_B becomes completely enshrouded in η_A's thick wind, preventing material at large distances ($\gtrsim 10a$) from being photoionized. As η_B emerges after periastron, the photoionization region is restored and grows as η_B moves back toward apastron. This plunging into, and withdrawal from, η_A's wind by η_B leads to the illumination of distant material in very specific directions as a function of phase.

3.3.4 *The emissivity equation*

For a simple two-level atom, the volume emissivity j (erg cm^{-3} s^{-1} sr^{-1}) of a forbidden line is

$$j = \frac{1}{4\pi} h\nu_{21} N_2 A_{21}, \quad (7)$$

where N_2 is the number density of atoms in the excited upper level and ν_{21} is the frequency of the line transition (Dopita & Sutherland 2003). Using the total number density of element of interest E in ionization state i, $n_{i,E} \approx N_1 + N_2$ (Ignace & Brimeyer 2006), together with equation (B5), one finds

$$N_2 = \left(\frac{n_e q_{12}}{n_e q_{21} + A_{21}}\right)(n_{i,E} - N_2). \quad (8)$$

Solving for N_2 and using equation (B4) for q_{21}/q_{12} gives

$$N_2 = n_{i,E}\left\{1 + \frac{g_1}{g_2}\exp\left(\frac{h\nu_{21}}{kT}\right)\left[1 + \frac{n_c}{n_e}\right]\right\}^{-1}, \quad (9)$$

where n_c, defined in equation (B6), is the critical density of the line. By defining $Q_{i,E} \equiv n_{i,E}/n_E$ as the fraction of element E in ionization state i, $A_E \equiv n_E/n_N$ as the abundance of element E relative to all nucleons n_N, and $\gamma_e \equiv n_N/n_e$ as the ratio of nucleons to electrons (Ignace & Brimeyer 2006), $n_{i,E}$ becomes

$$n_{i,E} = Q_{i,E} A_E \gamma_e n_e. \quad (10)$$

Therefore, using equations (9) and (10),

$$j = \frac{h\nu_{21} A_{21} Q_{i,E} A_E \gamma_e n_e}{4\pi} \times \left\{1 + \frac{g_1}{g_2}\exp\left(\frac{h\nu_{21}}{kT}\right)\left[1 + \frac{n_c}{n_e}\right]\right\}^{-1}. \quad (11)$$

Based on equation (11), emission from a specific forbidden line is concentrated only in regions that (1) contain the right ionization state of the element of interest (in our case, Fe^{2+}), (2) are near the critical

[4] The outer edge looks circular only because this marks the edge of the spherical computational domain of the SPH simulation.

density of the line (for [Fe III], $\sim 10^7\,\mathrm{cm}^{-3}$) and (3) are near the right temperature (for [Fe III], $T \approx 32\,000$ K). This important point is crucial to understanding the forbidden line emission observed in η Car.

To compute the emissivity using SPLASH, the line profiles are assumed to have a Gaussian thermal broadening, so that equation (11) is weighted by an exponential with the form

$$j = \frac{h\nu_{21} A_{21} Q_{\mathrm{i,E}} A_{\mathrm{E}} \gamma_{\mathrm{e}} n_{\mathrm{e}}}{4\pi} \exp\left[-\left(v_{\mathrm{bin}} - \frac{v_{\mathrm{los}}}{v_{\mathrm{th}}}\right)^2\right] \times \left\{1 + \exp\left(\frac{h\nu_{21}}{kT}\right)\left[\frac{g_1}{g_2} + \frac{A_{21} g_1 T^{1/2}}{\beta \Omega_{12} n_{\mathrm{e}}}\right]\right\}^{-1}, \quad (12)$$

where equation (B8) has been used for n_{c}, v_{los} is the line-of-sight velocity of material in the 3D SPH simulation for a specified orientation of the binary orbit relative to the observer, v_{th} is a thermal velocity dispersion (taken to be $25\,\mathrm{km\,s}^{-1}$) and v_{bin} is the bin size used along the dispersion axis of the synthetic slit in the wavelength range of interest, expressed in thermal velocity units ($25\,\mathrm{km\,s}^{-1}$).

To relate the physical density in the SPH simulation to the electron number density, we use $n_{\mathrm{e}} = \rho_{\mathrm{sph}}/(\mu_{\mathrm{e}} m_{\mathrm{H}})$, with μ_{e} the mean molecular weight per free electron. As the focus is on forbidden lines of trace metals, the value of n_{e} should not be impacted by the ionization balance of the metals (Ignace & Brimeyer 2006). Moreover, since far-UV radiation (or high-energy collisions) is necessary for the formation of the high-ionization forbidden lines, wherever [Fe III] emission occurs, hydrogen should also be ionized. For such regions dominated by H^+, we thus take $\mu_{\mathrm{e}} = \gamma_{\mathrm{e}} = 1$. The volume emissivity then takes the final general form

$$j = \frac{h\nu_{21} A_{21} Q_{\mathrm{i,E}} A_{\mathrm{E}} \rho_{\mathrm{sph}}}{4\pi m_{\mathrm{H}}} \exp\left[-\left(v_{\mathrm{bin}} - \frac{v_{\mathrm{los}}}{v_{\mathrm{th}}}\right)^2\right] \times \left\{1 + \exp\left(\frac{h\nu_{21}}{kT}\right)\left[\frac{g_1}{g_2} + \frac{A_{21} g_1 T^{1/2} m_{\mathrm{H}}}{\beta \Omega_{12} \rho_{\mathrm{sph}}}\right]\right\}^{-1}. \quad (13)$$

The appropriate value of $Q_{\mathrm{i,E}}$ is found assuming collisional ionization equilibrium, with the fraction of Fe^{2+} as a function of T based on the ion fraction data from Bryans et al. (2006). These data show that at $T \sim 250\,000$ K, the fractional abundance of Fe^{2+} is $10^{-5.453}$, with the remaining Fe being collisionally ionized to higher states. The amount of Fe^{2+} decreases even more at higher temperatures. The model therefore assumes zero [Fe III] emission from material with $T > 250\,000$ K.

3.3.5 *The intensity and synthetic slit spectroimages*

Since the [Fe III] emission is optically thin, the intensity I is simply the integral of the volume emissivity j along the line of sight,

$$I = \int j \, \mathrm{d}l \quad (14)$$

(Mihalas 1978). The intensity is computed in SPLASH by performing a line-of-sight integration of j through the entire 3D simulation at each pixel, resulting in an image of the intensity in the [Fe III] λ4659 line centred at a particular velocity (wavelength), as an observer would see it projected on the sky. This is done for multiple velocities (v_{bin}) in $25\,\mathrm{km\,s}^{-1}$ intervals for line-of-sight velocities from -600 to $+600\,\mathrm{km\,s}^{-1}$.

The resulting series of [Fe III] intensity images are combined using IDL routines to create a synthetic position versus velocity spectroimage. The IDL code reads in the SPLASH images and rotates them to a specified PA on the sky corresponding to a desired PA of the *HST*/STIS slit, assuming that the orbital axis is either aligned with the Homunculus polar axis at a $\mathrm{PA}_z = 312^\circ$, or rotated relative to the Homunculus axis by some specified angle. Each image is cropped to match the 0.1 arcsec width of the STIS slit, with the slit assumed centred exactly on the η Car central source. Since position information is only available along one direction, each image has its intensity values integrated along each row of pixels within the slit width. This produces a single 'slice' of the [Fe III] λ4659 intensity along the slit, centred at a specific velocity. These slices are combined to create the synthetic spectroimage.

The resulting model spectroimages have spatial (∼0.003 arcsec) and spectral ($25\,\mathrm{km\,s}^{-1}$) resolutions that are better than the *HST* observations. The synthetic spectroimages are therefore convolved with the response of *HST*/STIS in order to match its spatial (0.1 arcsec) and spectral ($37.5\,\mathrm{km\,s}^{-1}$) resolutions. Point spread functions (PSFs) for STIS generated using the TINY TIM program (Krist & Hook 1999) are used for the convolution in the spatial direction, while a Gaussian is used for the convolution in the spectral direction. Colour in the model spectroimages scales as the square root of the intensity, with the colour bar ranging from 0 to 1/4 of the maximum intensity, the same as used for displaying the observations.

Fig. 4 shows that there is a noticeable difference between the unconvolved (left) and convolved (right) model spectroimages, especially in the central ±0.15 arcsec. Details in the unconvolved spectroimages that arise near the inner WWC zone are completely unresolved in the convolved images, resulting in a bright, central streak of emission extending from negative to positive velocities. This is consistent with the observations and indicates that *HST*/STIS lacks the spatial resolution needed to resolve the details of η Car's inner WWC zone.

4 RESULTS FROM THE 3D DYNAMICAL MODEL

In the discussions below, it is assumed for simplicity that phase zero of the spectroscopic cycle (from the observations) coincides with phase zero of the orbital cycle (periastron passage). In a highly eccentric binary system like η Car, the two values are not expected to be shifted by more than a few weeks (Groh et al. 2010a). Such a time shift would only cause a small change of ∼10° in the derived best value of θ, which will not affect the overall conclusions.

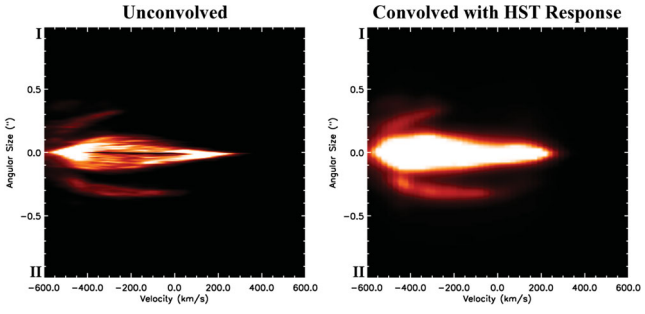

Figure 4. Example synthetic spectroimages of [Fe III] λ4659 both unconvolved (left) and convolved with the response of *HST*/STIS (right), assuming $i = 138^\circ$, $\theta = 0^\circ$ and $\mathrm{PA}_z = 312^\circ$. Roman numerals I and II indicate the top and bottom of the slit, respectively. Colour is proportional to the square root of the intensity, and the velocity scale is $\pm 600\,\mathrm{km\,s}^{-1}$.

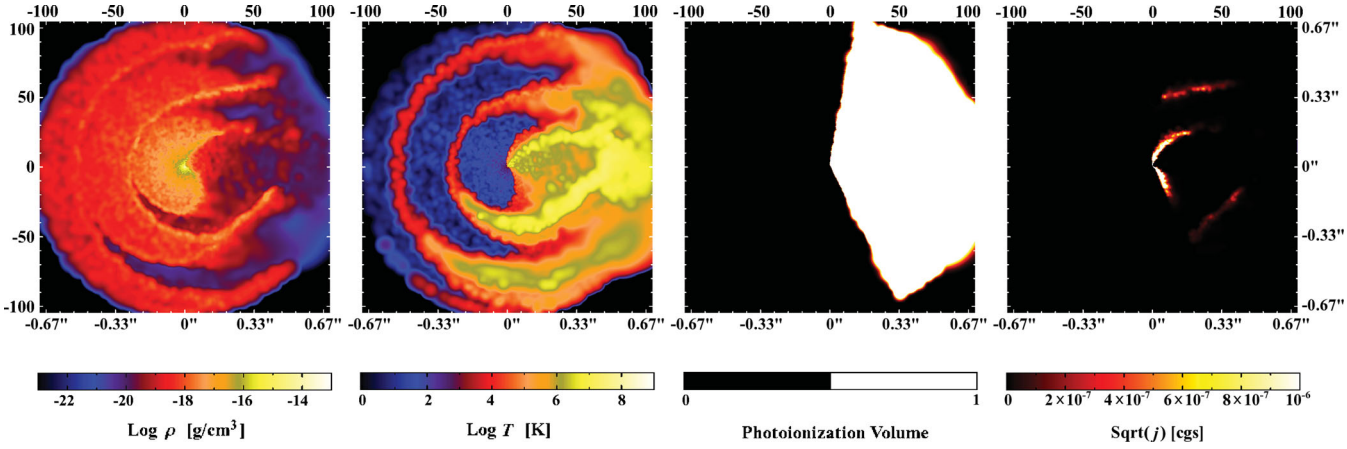

Figure 5. Snapshots in the orbital xy plane from the 3D SPH simulation of η Car at $\phi = 0.976$ used to model the observed blueshifted emission arcs of Fig. 2. Colour shows, from left to right, log density, log temperature, photoionization volume created by η_B (white = ionized) and square root of the modelled emissivity of the [Fe III] λ4659 line. The colour bar in the last panel has been adjusted to make faint emission more visible. The box size is $\pm 105a \approx \pm 1622$ au $\approx \pm 0.7$ arcsec ($D = 2.3$ kpc). Axis tick marks correspond to an increment of $10a \approx 154$ au ≈ 0.067 arcsec. In the last panel, [Fe III] emission only originates from material within the photoionization volume that is near the critical density of the [Fe III] line ($\sim 10^7$ cm^{-3}) and at the appropriate temperature.

4.1 Hydrodynamics of the extended WWC region

The first two columns of Figs 5 and 6 show, respectively, the density and temperature in the xy orbital plane from the 3D SPH simulation. The binary system has undergone multiple orbits, as indicated by the dense arcs of wind material in the outer ($>20a$) regions. On the $-x$ (periastron) side of the system are narrow cavities carved by η_B in η_A's dense wind during each periastron passage. The cavities are most easily seen in the temperature plots as they contain warm ($\sim 10^4$–10^5 K), low-density wind material from η_B. Bordering these cavities are compressed, high-density shells of primary wind that form as a result of the WWC.

The insets of Fig. 6 illustrate the creation of one of these narrow wind cavities and its bordering dense shell of primary wind. Their spiral shape is due to the increased orbital speeds of the stars during periastron. This is in contrast to phases around apastron (rows b, c and d) when orbital speeds are much lower and the current WWC zone maintains a simple, axisymmetric conical shape (O08; P09, P11). The increasing orbital speeds when approaching periastron causes the post-shock gas in the leading arm of the WWC zone to be heated to higher temperatures than the gas in the trailing arm (insets of rows d and e), an affect also found by P11.

Following periastron, η_B moves back to the $+x$ (apastron) side of the system, its wind colliding with and heating the dense primary wind that flows unimpeded in the $+x$, $-y$ direction. As pointed out by P11, the arms of the WWC region shortly after this ($\phi \approx 0.1$) are so distorted by orbital motion that the leading arm collides with the trailing arm from before periastron, leading to additional heating of the post-shock gas in the trailing arm (compare $\phi \approx 1.122$, Fig. 6, row f). The leading arm of the WWC zone (including the portion that collides with the trailing arm) helps to form a dense, compressed shell of primary wind that flows in the $+x$ and $-y$ directions after periastron passage. Because the wind of η_B collides with a dense wall of post-shock primary wind with high inertia, the primary wind controls the overall rate of expansion of the resulting spiral (P11).

The overall stability of the expanding shell of primary wind on the apastron side of the system depends on the shock thickness (Vishniac 1983; Wünsch et al. 2010; P11). Portions of the shell moving in the $-y$ direction appear to be the most stable due to the increased amount of primary wind that borders it in this direction. However, our simulations show that at $\phi \approx 0.3$, the upper portion of the shell expanding in the $+x$, $+y$ direction starts to fragment. Eventually, the wind of η_B is able to plough through the shell, causing it to separate from the leading arm of the WWC zone ($\phi \approx 0.4$, row c of Fig. 6). This produces a pair of dense 'arcs' of primary wind on the apastron side of the system. The arc expanding in the $+x$, $-y$ direction is the remnant of the leading arm of the WWC region from the previous periastron passage. The arc in the $+x$, $+y$ direction is the remnant of the trailing arm of the WWC region from just *prior* to the previous periastron passage. Multiple pairs of these arcs are visible in Figs 5 and 6. They are also quite spatially extended; by the time the system is back at periastron, the arcs from the previous periastron are up to $70a$ from the central stars (in the xy plane). As the arcs expand further, they gradually mix with the surrounding low-density wind material from η_B.

The fragmentation of the shell and formation of the arcs is mainly due to the above-mentioned collision of the leading arm of the WWC zone with the trailing arm just after periastron. This collision produces instabilities at the interface between the two arms (P11), which, together with the shell's expansion, the pressure from η_B's high-velocity wind, and the lack of bordering primary wind material for support, causes the shell to break apart in the $+x$, $+y$ direction ~ 1.7 yr after periastron.

While the term 'shell' is used to describe the layer of compressed primary wind that flows in the direction of apastron following periastron passage, this is not related to the 'shell ejection' event discussed in the past η Car literature (Zanella, Wolf & Stahl 1984; Davidson 1999, 2005; Davidson et al. 1999; Smith et al. 2003). The scenario proposed by Zanella et al. (1984) and advocated by Davidson (1999) to explain η Car's spectroscopic events is a qualitative single-star model wherein some sort of thermal or surface instability is presumed to induce significant mass loss from η Car approximately every 5.54 yr. A shell ejection as the result of a latitude-dependent disturbance in the wind of a single star has also been proposed (Smith et al. 2003; Davidson 2005). Davidson (2005) suggested that the shell event may be triggered by the close approach of a secondary star, but this is still mainly a single-star scenario requiring some kind of surface instability in the primary.

In contrast to these ideas, the formation of the outflowing shell of primary wind seen in the 3D SPH simulations is a natural,

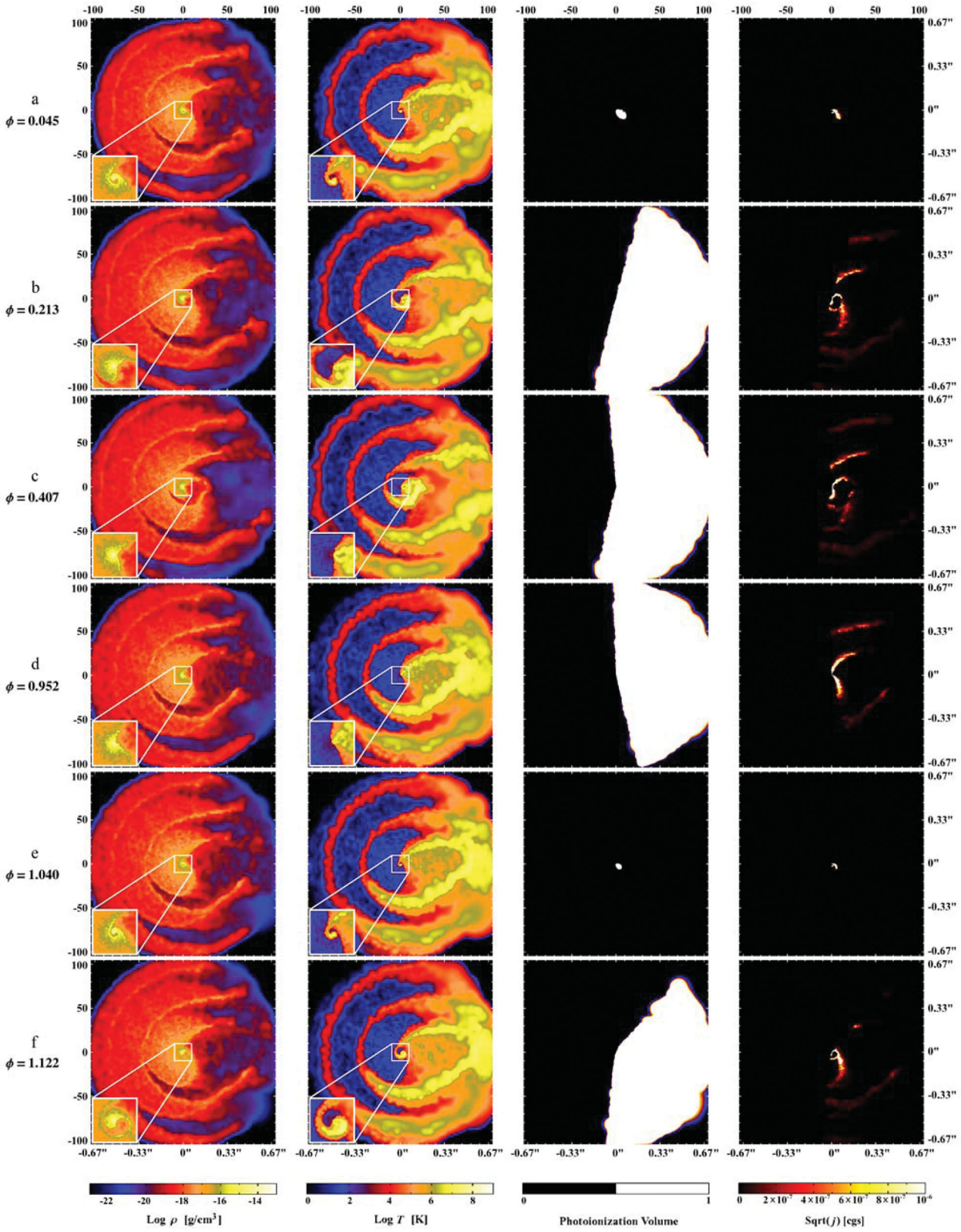

Figure 6. Same as Fig. 5, but for $\phi = 0.045$, 0.213, 0.407, 0.952, 1.040 and 1.122 (rows, top to bottom), which correspond to phases at which *HST*/STIS observations were accomplished (fig. 11 of G09). Insets in the first two columns are a zoom of the inner 10a, included to illustrate the complex dynamics of the 'current' WWC region.

unavoidable consequence in any high-eccentricity, massive CWB in which the primary star has a significant mass-loss rate (significant both in terms of overall mass-loss rate and mass-loss rate relative to the companion star). It is not so much an 'ejection' event as it is a chance for the normal primary wind to flow in the direction of apastron for a brief time (∼3–5 months) while η_B performs periastron passage. Eventually, η_B returns to the apastron side and its high-velocity wind collides with and compresses this primary wind material, forming a dense shell that continues to propagate in the direction of apastron until it breaks apart at its weakest point, resulting in a pair of dense 'arcs', as described above.

4.2 Physical origin and location of the broad high-ionization forbidden line emission

Fig. 5 presents slices in the orbital plane from the 3D SPH simulation at $\phi = 0.976$, used to model the blueshifted emission arcs seen at STIS slit PA $= +38^\circ$. The colours show log density, log temperature, photoionization zone created by η_B and square root of the modelled emissivity of the [Fe III] λ4659 line. The photoionization region is confined to the same side of the system as η_B, the dense wind of η_A preventing the far ($-x$) side of the system from being photoionized. All of the [Fe III] emission is thus concentrated in two spatially distinct regions on the apastron side of the system.

(i) The strongest [Fe III] emission originates near the walls of the current WWC zone in the inner $\sim 30a \approx 0.2$ arcsec of η Car.

(ii) Faint, spatially extended (out to $\sim 60a \approx 0.4$ arcsec) [Fe III] emission arises in the arcs of dense primary wind formed during the previous periastron passage.

The [Fe III] emission occurs in these two areas because they are the regions within the photoionization zone that are near the critical density of the [Fe III] line and at the appropriate temperature.

Fig. 6 illustrates how the density, temperature, photoionization region and [Fe III] λ4659 emissivity change with orbital phase. The six phases shown correspond to those observed in fig. 11 of G09. During periastron passage ($\phi = 0.045$ and 1.040, rows a and e), η_B becomes deeply embedded in the dense wind of η_A and the photoionization region shrinks considerably, down to only a few semimajor axes across. This leads to an effective 'shutting-off' of the forbidden line emission at large distances ($\gtrsim 10a$). By $\phi = 0.213$ and 1.122 (rows b and f), η_B has moved far enough from η_A to re-establish the large photoionization zone and spatially extended forbidden line emission. The photoionization region is largest, and the [Fe III] most spatially extended, around apastron (row c, $\phi = 0.407$). By $\phi = 0.952$ (row d), η_B starts to become embedded in the dense wind of η_A, the photoionization region in the $+x$, $-y$ quadrant decreasing slightly in size.

Far-UV radiation from η_B leads to highly ionized regions that extend outward from its low-density wind cavity in the direction of system apastron. During periastron passage, the disappearance of the extended high-ionization forbidden emission can be attributed to the wrapping of the dense primary wind around η_B, which traps its far-UV radiation and prevents it from photoionizing the outer wind structures responsible for the observed emission. While η_B is embedded in η_A's wind, the latter flows unimpeded in the direction of apastron, eventually forming dense arcs of material that expand outward as η_B completes periastron passage and the inner regions of the WWC zone regain their near conical shape. These cooler, dense arcs of expanding primary wind also produce high-ionization forbidden line emission when photoionized by η_B.

Observed temporal variations of the high-ionization forbidden lines can thus be linked to the orbital motion of η_B in its highly eccentric orbit, which causes different portions of the WWC regions and extended arcs of primary wind from earlier cycles to be photoionized. As the two stars move closer to or farther from each other, orbital motion also leads to changes in the density and temperature of the inner WWC zone, which in turn modifies the size and shape of η_B's photoionization volume, and thus the overall shape, location and intensity of the high-ionization forbidden line emission, even at phases away from periastron (rows b, c, d and f of Fig. 6). Forbidden line emission from the compressed, inner WWC region increases in intensity until the critical density is reached or the temperature exceeds that at which the appropriate ions can exist. Forbidden emission from the extended arcs of primary wind decreases in intensity as the arcs gradually expand and mix with the surrounding low-density wind material from η_B.

4.3 Synthetic slit spectroimages and constraining the orbital orientation

4.3.1 Constraint 1: emission arcs at slit PA $= +38^\circ$, $\phi = 0.976$

The blueshifted emission arcs in Fig. 2 represent distinct, well-defined structures observed at a specific orbital phase and slit PA. As such, they provide a natural basis for modelling and can be used to constrain the orbital orientation. We have performed a parameter study in i, θ and PA_z with the goal of determining which set(s), if any, of orientation parameters result in synthetic spectroimages that closely match the observations in Fig. 2. The value of θ was varied in 15° increments for values of $0^\circ \leq \theta \leq 360^\circ$, with i varied in 5° increments over the range $0^\circ \leq i \leq 180^\circ$ for each θ value, and PA_z varied in 5° increments over the range $0^\circ \leq PA_z \leq 360^\circ$ for each pair of i, θ values.

Only synthetic spectroimages generated for $-15^\circ \leq \theta \leq +45^\circ$ are able to reasonably match the observations taken at $\phi = 0.976$, PA $= 38^\circ$. However, an ambiguity exists in i and PA_z, with values of $30^\circ \leq i \leq 50^\circ$, $PA_z = 272^\circ$ to 332° (top row of Fig. 7) and $130^\circ \leq i \leq 150^\circ$, $PA_z = 282^\circ$ to 342° (bottom row of Fig. 7) both capable of producing entirely blueshifted arcs that resemble those observed. Our best morphological fits are obtained using values of $i = 42^\circ$, $\theta = 7^\circ$, $PA_z = 302^\circ$ or $i = 138^\circ$, $\theta = 7^\circ$, $PA_z = 317^\circ$, which lie near the centres of these two derived ranges of best-fitting orientation parameters.

The observed morphology and asymmetries in brightness and v_{los} of the spatially extended emission arcs determine the allowed ranges of the orbital orientation parameters. The parameters i and PA_z primarily control the brightness asymmetry and spatial orientation of the blue- and redshifted emission components on the sky. Fig. 7 shows that the synthetic spectroimages at slit PA $= 38^\circ$ for $i = 42^\circ$ and 138° (at nearly identical θ and PA_z) are remarkably similar. Yet, the two orbital orientations are drastically different, resulting in unique distributions on the sky of the blue- and redshifted emission. The red component is the most notable, which extends to the SE for $i = 42^\circ$, but to the NW for $i = 138^\circ$. The asymmetry in brightness between the two blueshifted arcs is also controlled by i. Only values of $30^\circ \leq i \leq 50^\circ$ or $130^\circ \leq i \leq 150^\circ$ produce a brightness asymmetry, with other i resulting in arcs that are approximately equal in brightness.

The value of PA_z determines the final orientation of the projected z-axis, and thus of the individual emission components. Because the lower blueshifted arc in the observations is brighter than the upper arc, the extended blue emission projected on the sky must be

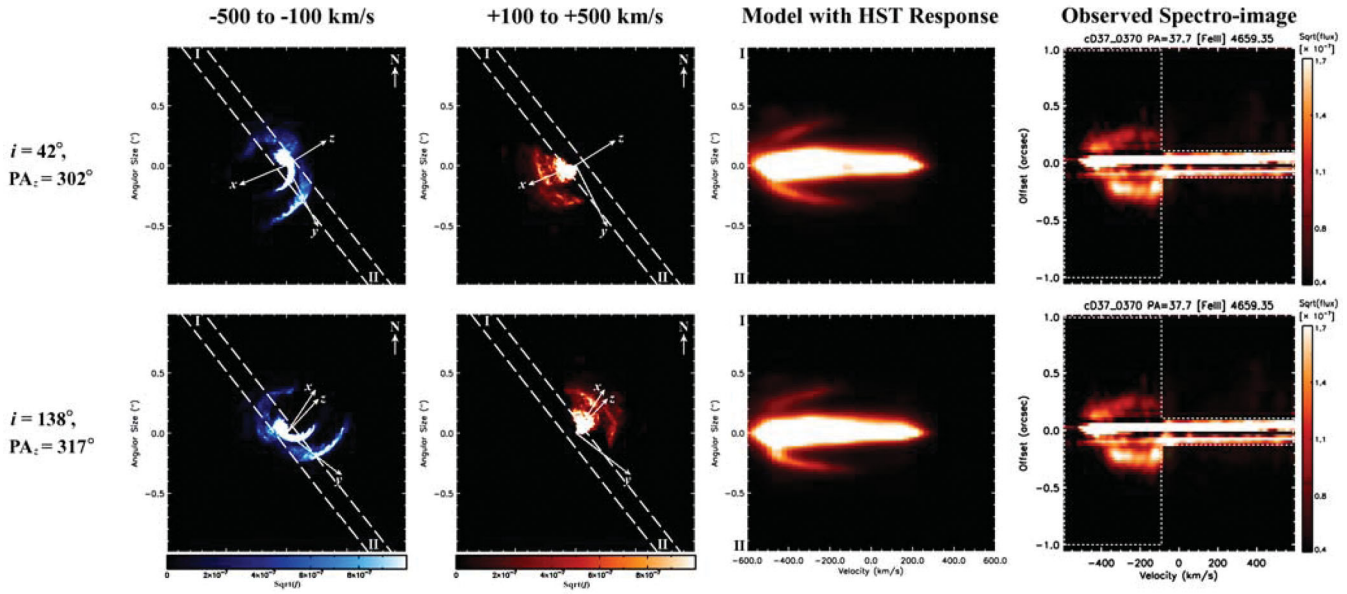

Figure 7. 2D spatial distribution on the sky of the square root of the modelled intensity in the [Fe III] λ4659 line and synthetic spectroimages for orbital orientations $i = 42°$, $\theta = 7°$, $PA_z = 302°$ (top row) and $i = 138°$, $\theta = 7°$, $PA_z = 317°$ (bottom row), which lie near the centres of the two derived best-fitting ranges of orientation parameters for matching the observations taken at $\phi = 0.976$, PA = 38° in Fig. 2. Columns are, from left to right: 2D distribution on the sky of the square root of the modelled intensity in the [Fe III] λ4659 line for blueshifted material with v_{los} between −500 and −100 km s^{-1}; same as first column, but for redshifted material with v_{los} between +100 and +500 km s^{-1}; model spectroimage convolved with the response of *HST*/STIS and observed spectroimage with mask. The projected *x*, *y* and *z* axes are shown for reference in the 2D images of the intensity on the sky, as is the direction of north. The 0.1 arcsec wide STIS slit at PA = +38° is also overlaid. Roman numerals I and II indicate the top and bottom of the slit, respectively. All following 2D projections of the modelled [Fe III] intensity in this paper use this same labelling convention. The colour scale in the spectroimages is proportional to the square root of the intensity and the velocity scale is ±600 km s^{-1}. Lengths are in arcseconds.

brighter in directions to the SW (where the lower half of the slit is located, position II in Fig. 7), and dimmer in directions to the NE (position I). This limits PA_z to values between 272° and 342°.

More importantly, *i* and PA_z determine the 3D orientation of the orbital axis. If $i = 42°$ and $PA_z = 272°$ to 342°, the orbital axis is inclined toward the observer and *is not aligned* with the Homunculus polar axis. The two stars would also orbit counter-clockwise on the sky. However, if $i = 138°$, then, because $PA_z \approx 312°$, the orbital axis *is* closely aligned *in 3D* with the Homunculus polar axis, and the stars orbit clockwise on the sky.

Fig. 8 shows that the value of θ (for fixed $i = 138°$ and $PA_z = 312°$) determines the v_{los} of the material exhibiting [Fe III] emission. According to our 3D model, the spatially extended [Fe III] emission originates in the expanding arcs of dense primary wind formed during the previous periastron passage. When $\theta \approx 0°$ (top row of Fig. 8) this emission is mostly blueshifted because the emitting material within η_B's photoionization zone is moving mostly toward the observer. The model spectroimage consists of spatially extended, blueshifted arcs because the slit at PA = 38° primarily samples the blue component, which stretches from NE to SW on the sky. In contrast, the extended red component is *not* sampled; only a small amount of redshifted emission in the very central ±0.1 arcsec core falls within the slit. Moreover, only values of $-15° \leq \theta \leq +45°$ produce significant amounts of spatially extended (∼0.7 arcsec in total length) blueshifted emission with the correct observed asymmetry in v_{los}, wherein the dimmer upper arc extends ∼75 km s^{-1} more to the blue than the brighter lower arc.

Fig. 7 demonstrates that our 3D dynamical model and derived best-fitting orbital orientation(s) reproduce all of the key features in the observations taken at $\phi = 0.976$, PA = 38°. Both synthetic and observed spectroimages contain concentrated, velocity-extended emission in the central ±0.1 arcsec core. The completely blueshifted emission arcs extend to roughly the same spatial distances (∼± 0.35 arcsec). The asymmetry in brightness between the upper and lower arcs is matched as well. The asymmetry in v_{los} is also reproduced and of the same magnitude. However, the arcs in the model images stretch a bit farther to the blue, to ∼−550 (upper arc) and −475 km s^{-1} (lower arc), versus ∼−475 and −400 km s^{-1} in the observations. The synthetic images thus show emission at velocities slightly above the value used in the SPH simulation for η_A's wind terminal speed. This is a minor discrepancy though, likely due to the extended emitting material receiving an extra 'push' from the fast wind of η_B (see Section 4.3.4).

4.3.1.1 Results for orbital orientations with a $\theta \approx 180°$. Returning back to Fig. 8, one sees that the spectroimage for $\theta = 180°$ fails to match the observations. There is a distinct lack of any spatially extended, blueshifted emission. Instead, the extended emission arcs are entirely *redshifted* due to the quite different v_{los} of the emitting material. When $\theta = 180°$, η_A is between the observer and η_B during most of the orbit. Therefore, all of the emitting material within η_B's photoionization zone is on the far side of the system and moving *away from* the observer. The extended forbidden line emission is thus mostly redshifted. The slit at PA = 38° now primarily samples this red component, producing a spectroimage consisting of entirely redshifted, spatially extended arcs, the direct *opposite* of the observations.

Changing the value of *i* and/or PA_z when $\theta = 180°$ does not result in a better match to the observations since most of the material photoionized by η_B and exhibiting forbidden line emission is still moving away from the observer. This is true for all values of θ near 180°; none of the model images generated for $135° \leq \theta \leq 225°$,

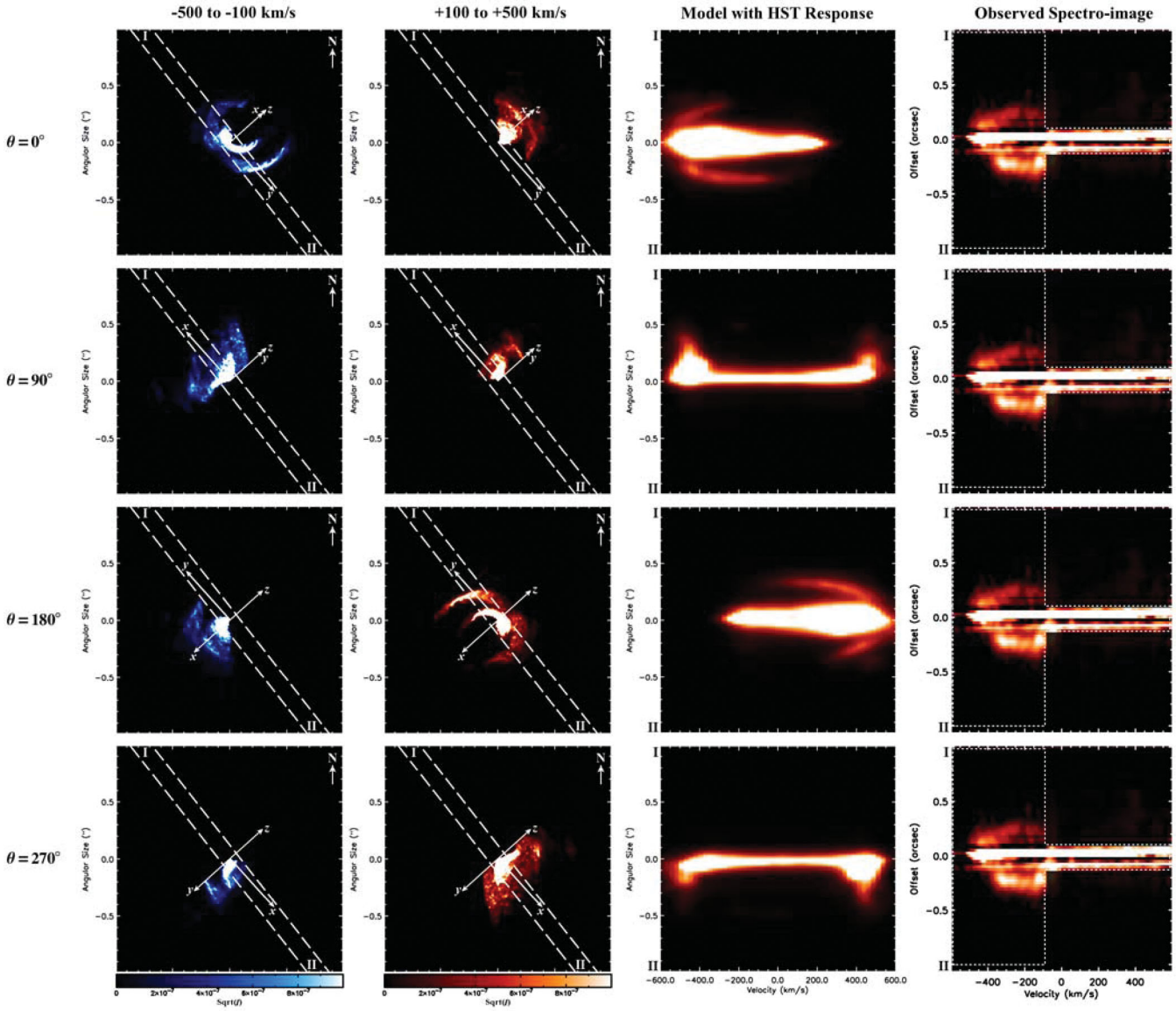

Figure 8. Same as Fig. 7, but for values of $\theta = 0°, 90°, 180°$ and $270°$ (rows, top to bottom), assuming $i = 138°$ and $\mathrm{PA}_z = 312°$.

regardless of the assumed i and PA_z, matches the $\phi = 0.976$, PA $= 38°$ observations. Example model spectroimages for these orientations can be found in Madura (2010). We therefore find that an orbital orientation that places η_B on the near side of η_A at periastron, such as that favoured by Falceta-Gonçalves et al. (2005), Abraham et al. (2005), Abraham & Falceta-Gonçalves (2007), Kashi & Soker (2007, 2008), Falceta-Gonçalves & Abraham (2009) and others, is explicitly ruled out.

4.3.1.2 Results for orientations with $\theta \approx 90°$ and $270°$. Model spectroimages for $\theta = 90°$ and $270°$ also fail to match the observations. The 2D images of the modelled [Fe III] intensity on the sky in Fig. 8 show that in both cases, one half of the STIS slit is empty (from centre to position II for $\theta = 90°$ and from I to the centre for $\theta = 270°$). Therefore, emission is absent to one side spatially in the spectroimages. Changing the value of i has no effect on this since a change in i at these θ values is equivalent to a rotation about the x-axis in the 2D intensity images. Instead, a rotation of nearly 90° in PA_z is needed in order to place emitting material in both halves of the slit. However, such a rotation does not result in a match to the observations. Synthetic spectroimages for $45° < \theta < 135°$ and $225° < \theta < 345°$ all suffer from the same problems, namely, either no blueshifted ring-like emission feature (if $\mathrm{PA}_z \approx 132°$ or $312°$), or arc-like emission to only one side spatially (if $\mathrm{PA}_z \approx 42°$ or $222°$) (Madura 2010). This is true regardless of the i and PA_z assumed.

4.3.2 Constraint 2: variations with phase at slit PA $= -28°$

Using the 3D dynamical model we generated synthetic spectroimages for a slit PA $= -28°$ at each of the phases in fig. 11 of G09, $\phi =$ 0.045, 0.213, 0.407, 0.952, 1.040 and 1.122. The main goals were to determine if the binary scenario and 3D model could explain the phase dependence observed in the high-ionization forbidden lines, and whether the set of PA $= -28°$ observations could resolve the ambiguity between the sets of $i = 35°$ to $50°$ and $i = 130°$–$145°$ best-fitting orientations found in the above subsection.

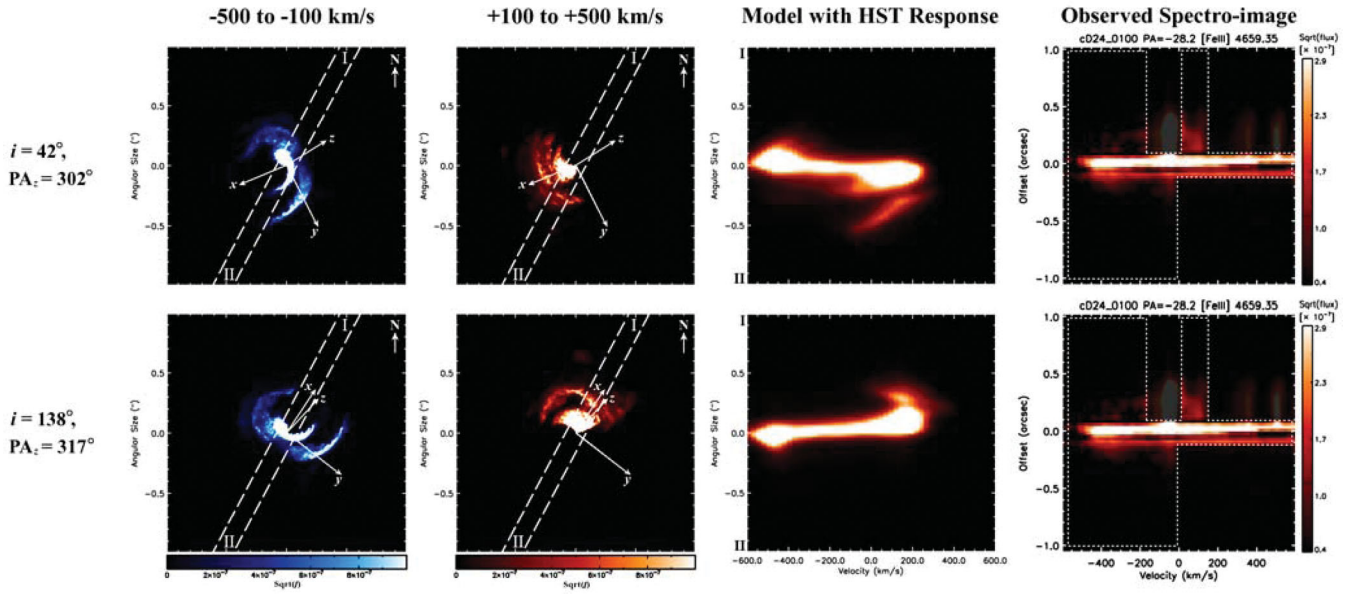

Figure 9. Same as Fig. 7, but for $\phi = 0.952$, slit PA $= -28°$. Note that the red- and blueshifted emission in the model spectroimage that assumes $i = 42°$ (top row) spatially extends in the wrong directions compared to the observations. η Car's orbital orientation parameters are thus constrained to values of $i \approx 130°$ to $145°$, $\theta \approx 0°$ to $15°$, $\mathrm{PA}_z \approx 302°$ to $327°$ (see text).

Fig. 9 illustrates the results of investigating the two best-fitting i regimes. It is clear that synthetic spectroimages for $i \approx 30°$ to $50°$ *do not* match the observations taken at slit PA $= -28°$ (top row of Fig. 9). There are a number of discrepancies, but the most important and obvious is that the blue- and redshifted emission components in the synthetic spectroimage extend in the wrong spatial directions, with the blue emission stretching to the NW and the red to the SE, the *opposite* of the observations.

In contrast, synthetic images generated for $i \approx 130°$ to $150°$ (bottom row of Fig. 9) *are* capable of matching the observations. The morphology of the PA $= -28°$ observations breaks the degeneracy in i and fully constrains, in 3D, η Car's orbit. Because redshifted emission is observed to extend spatially in directions to the NW, the red emission component of [Fe III] on the sky must be oriented such that it too stretches NW and falls within the top half of the PA $= -28°$ slit. The synthetic images of the [Fe III] intensity on the sky (first two columns of Figs 9 and 10) illustrate how the slit at PA $= -28°$ samples the emitting regions of η Car's extended interacting winds in very different directions compared to slit PA $= 38°$. This is why the observed spectroimages are so different between the two slit PAs, even at similar orbital phases. We find that *only* orbital orientations with $i \approx 130°$ to $145°$, $\theta \approx 0°$ to $15°$, $\mathrm{PA}_z \approx 302°$ to $327°$ are able to simultaneously match the observations taken at both slit PA $= 38°$ *and* $-28°$.

Fig. 10 shows that the 3D dynamical model and derived orbital orientation reproduce the overall observed shape and velocity structure of the [Fe III] emission at each phase for slit PA $= -28°$. Fig. 10 further illustrates how η Car's extended interacting winds change with time. The orientation of the blue component does not appear to change, always stretching from NE to SW on the sky. However, the spatial extent does change, growing larger going from periastron to apastron as the wind structures flow outward. Moving from apastron back to periastron, the intensity and spatial extent of the blue component eventually start to decrease as the expanding arcs of primary wind drop in density and mix with the surrounding wind from η_{B}. The redshifted emission changes in a way similar to that of the blue component, but points mainly NW.

4.3.3 *Constraint 3: observed variations with φ and slit PA*

Synthetic spectroimages were generated at the 10 combinations of phase and slit PA in Table 2, assuming the best-fitting orientation $i = 138°$, $\theta = 7°$ and $\mathrm{PA}_z = 317°$. The goal was to determine how well the 3D model and derived binary orientation could reproduce observations at a variety of other phases and slit PAs. Model images for $\phi = 1.001$ and 1.013 are nearly identical to those at $\phi = 0.045$ and 1.040 in Fig. 10 and add no new information. We therefore focus this discussion on the phases before and after periastron.

Fig. 11 presents the results. The overall match between synthetic and observed spectroimages is quite good. The model reproduces all of the key spatial features, namely, extended ($>\pm$ 0.1 arcsec) [Fe III] emission that is almost entirely blueshifted for positive slit PAs, but that is partially redshifted for negative slit PAs. Observed variations in emission with phase are also reproduced.

Model images at $\phi = 0.601$ (Fig. 11a) and 0.738 (Fig. 11b) demonstrate how a large change in slit PA results in very different spectroimages. The spatial distributions of the emission on the sky are very similar at these two phases, as expected since the system is near apastron when orbital velocities are their lowest. However, the slit at PA $= -82°$ samples the emission in very different directions compared to PA $= 22°$, producing a spectroimage that resembles those taken at PA $= -28°$ in Fig. 10.

The partial ring of emission observed at $\phi = 0.984$, PA $= 62°$ (Fig. 11f), is also noteworthy. The match between model and observations is very good, the emission arc to the SW present in both, as well as the much shorter arc to the NE between ~ -500 and $-350\,\mathrm{km\,s^{-1}}$. Two effects appear to be causing the NE arc to be shorter. First, due to their outward expansion, the extended arcs of primary wind have dropped in density and started to mix with the

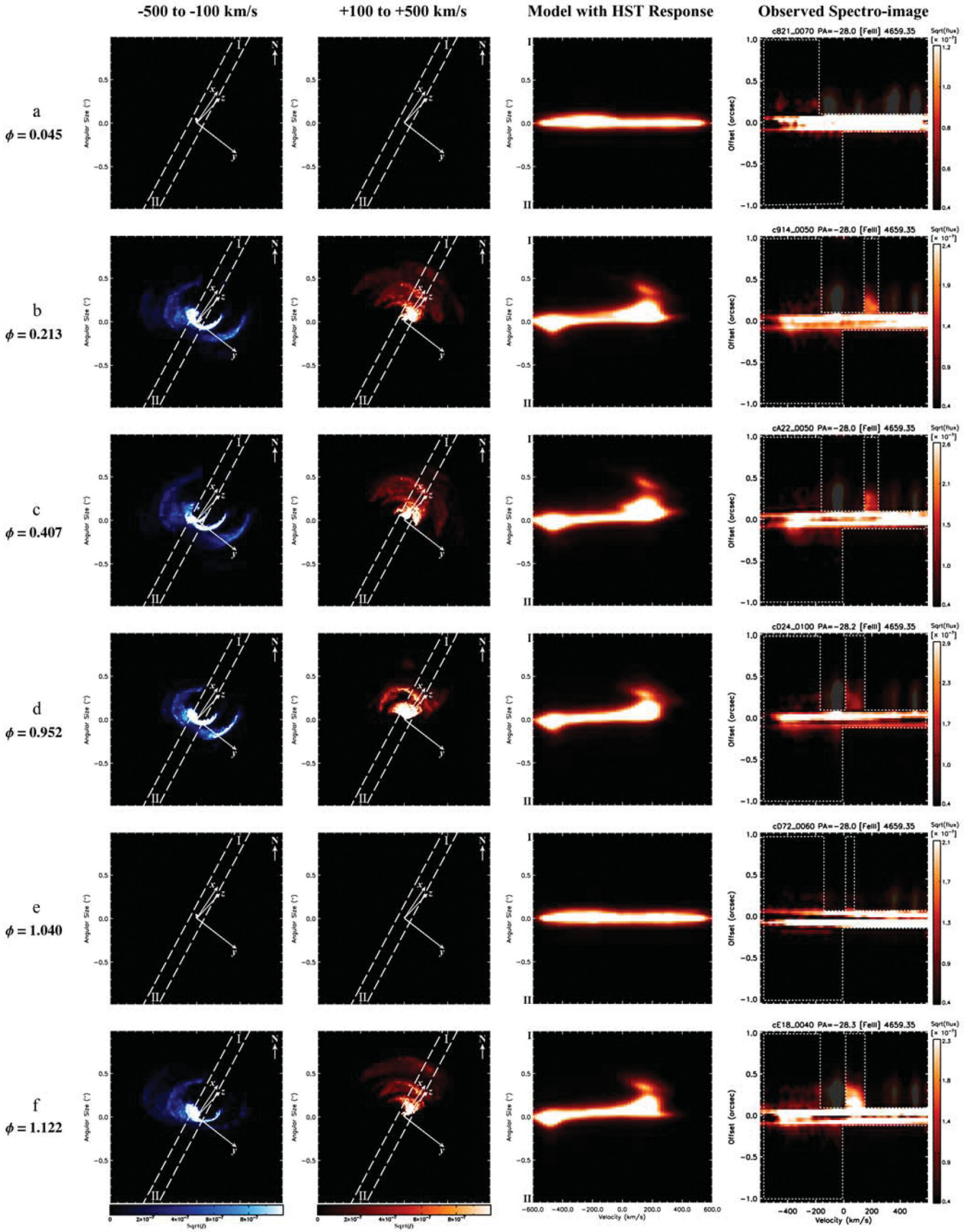

Figure 10. Same as Fig. 7, but for phases (rows, top to bottom) $\phi = 0.045$, 0.213, 0.407, 0.952, 1.040 and 1.122, with the STIS slit at PA $= -28^\circ$ (as in fig. 11 of G09), and assuming $i = 138^\circ$, $\theta = 7^\circ$, $\mathrm{PA}_z = 317^\circ$.

Table 2. Phases and slit PAs from figs 12 and 13 of G09 modelled in Section 4.3.3 and shown in Fig. 11.

ϕ	PA	Fig.
0.601	+22°	11(a)
0.738	−82°	11(b)
0.820	+69°	11(c)
0.930	−57°	11(d)
0.970	+27°	11(e)
0.984	+62°	11(f)
0.995	+70°	11(g)
1.001	+69°	–
1.013	+105°	–
1.068	−142°	11(h)

surrounding low-density wind from η_B. Second, the photoionization of material in directions to the NE by η_B has diminished due to its clockwise orbital motion and gradual embedding in η_A's wind. These lead to a decrease in the amount of extended [Fe III] emission to the NE. This, combined with the slit PA, produces a partial arc of blueshifted emission to the NE in the spectroimage.

By $\phi = 0.995$ (Fig. 11g), the extended emission has vanished, implying that the ionizing flux of photons from η_B shuts off sometime between $\phi = 0.984$ and 0.995. At $\phi = 1.068$ (Fig. 11h), there is still no observed spatially extended emission. Yet, the 2D model images of the intensity on the sky show that the extended [Fe III] emission has started to return in directions to the NE. This is visible in the model spectroimage as a bright, blueshifted bulge that points NE. Unfortunately, the observational data in the central ±0.15 arcsec is of insufficient quality to tell if such an emission bulge was detected.

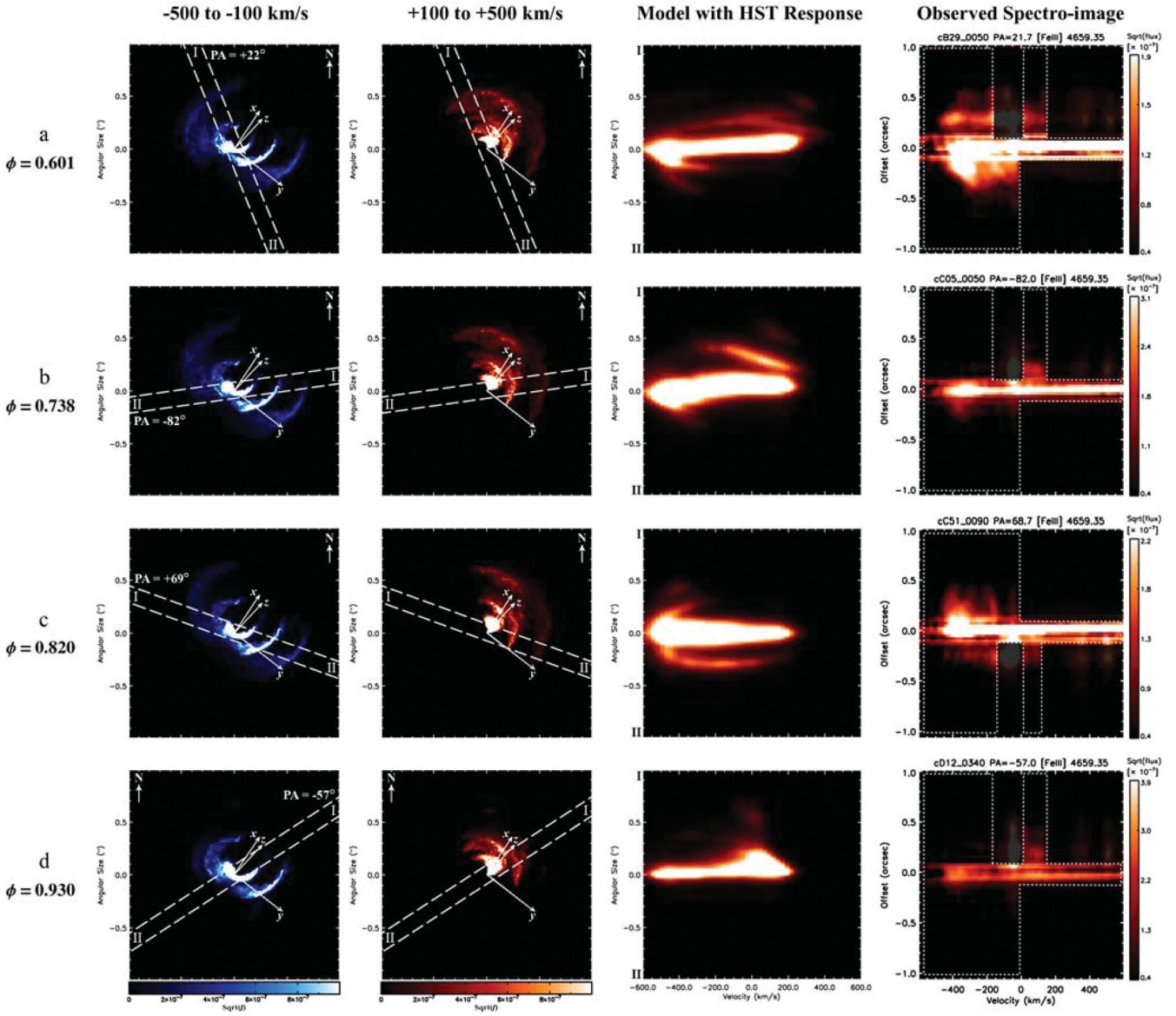

Figure 11. A – Same as Fig. 10, but for the observed orbital phases and STIS slit PAs listed in Table 2. Phases are (top to bottom): $\phi = 0.601$, 0.738, 0.820 and 0.930. The 0.1 arcsec wide STIS slit is shown overlaid at the appropriate PA in the 2D images of the modelled intensity on the sky. Roman numerals I and II indicate the top and bottom of the slit, respectively. B – Same as Fig. 11A, but at phases (top to bottom) $\phi = 0.970$, 0.984, 0.995 and 1.068.

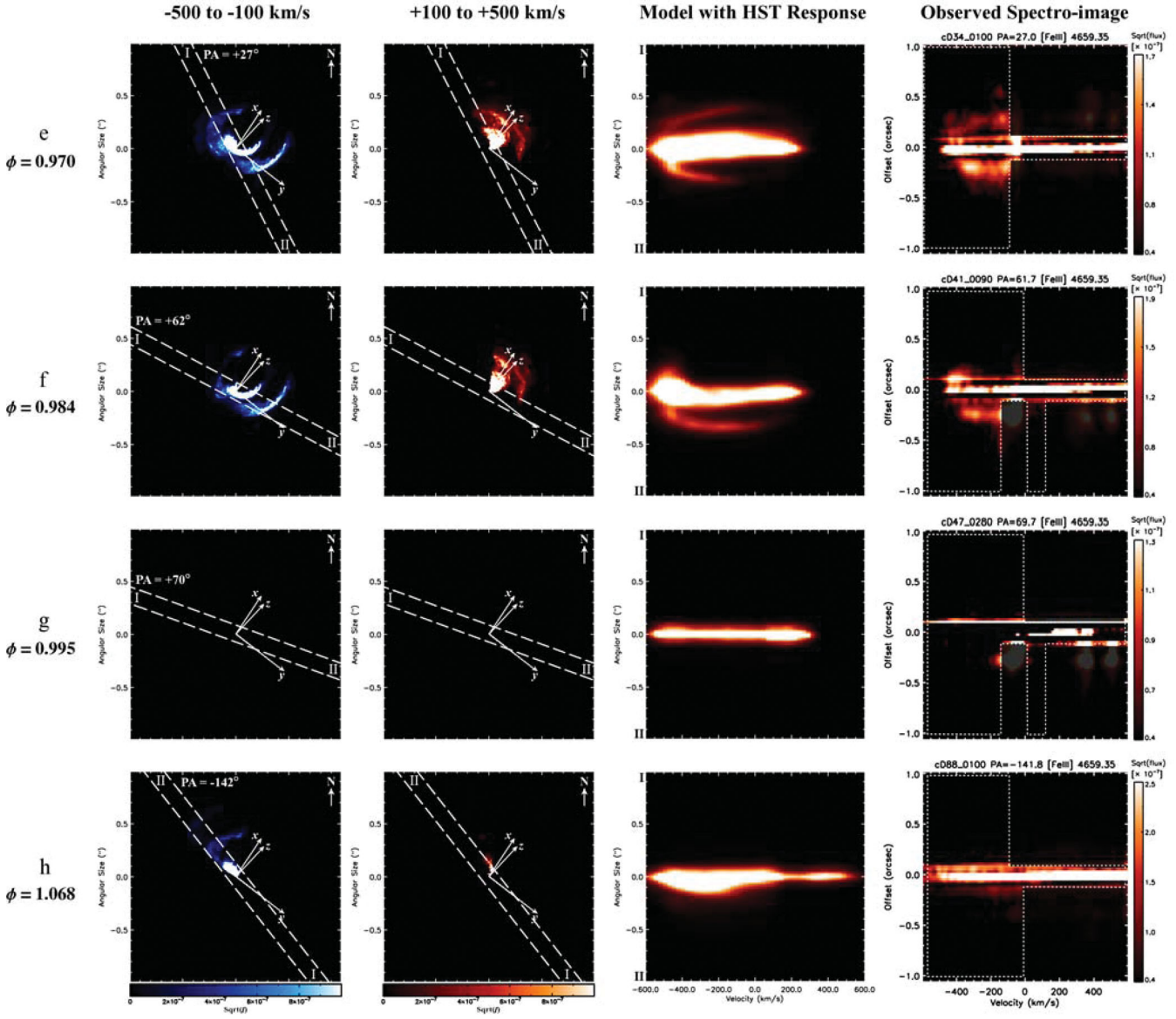

Figure 11 – *continued*

Nevertheless, the 3D model predicts that η_B should start to emerge from η_A's dense wind and begin to restore the spatially extended, high-ionization forbidden line emission at $\phi \approx 1.068$.

4.3.4 Discrepancies between the observations and 3D model

During most of the orbit, the wind of η_B collides with the dense arcs of primary wind on the apastron side of the system where the spatially extended forbidden line emission forms (see rows b through d of Fig. 6). Because the arcs are bordered by a large, low-density wind cavity created earlier by η_B, they have almost no support against η_B's high-velocity wind, which is able to drive portions of the arcs into the cavity at velocities just above their outflow speed, the terminal speed of the primary wind. An orientation that places the observer on the apastron side of the system thus results in model spectroimages containing blueshifted emission at velocities slightly higher than the wind terminal velocity of the primary.

Because the observations do not contain blueshifted emission at speeds more than $\sim$500 km s^{-1}, the wind speed(s) of η_A and/or η_B used in the SPH simulation may be a bit too large. The launching of the two winds at their terminal velocity in the simulation may also be having a small effect on the results. Better constraints on η_B's wind terminal speed and improved 3D simulations with proper driving of the stellar winds should help resolve these issues. Improved modelling coupled with future observations of the extended forbidden emission in η Car's central arcsecond also has the potential to further constrain the wind terminal velocity of η_A.

The main discrepancies between synthetic spectroimages assuming $i = 138°$, $\theta = 7°$, $PA_z = 317°$ and the observations for slit PA $= -28°$ are (1) the extended blueshifted component is located $\sim$100 km s^{-1} farther to the blue in the model images than in the observations, and (2) the redshifted component in the model images is $\sim$75 km s^{-1} broader than observed. Both issues are likely due to the reasons discussed above concerning the wind terminal velocities of η_A and η_B.

5 DISCUSSION

5.1 The orientation and direction of η Car's binary orbit

There has been much speculation about the binary orientation, and many papers published offering suggestions (see Section 1). The detailed modelling of Section 4 tightly constrains the observer's line of sight to angles of $\theta \approx 0^\circ$–15° prograde of the semimajor axis on the apastron side of the system, placing η_B behind η_A during periastron. Given the uncertainties in the stellar and wind parameters of η_B used in the 3D simulations, and the assumption that phase zero of the orbital and spectroscopic periods coincide, values of $-15^\circ \lesssim \theta \lesssim +30^\circ$ may also be possible. A study in the stellar/wind parameters of η_B, or improved observational constraints, is needed to further refine the value of θ.

More importantly, the results bound, for the first time, the orientation of η Car's orbital plane, with the orbital axis closely aligned in 3D with the inferred polar axis of the Homunculus at an $i \approx 130^\circ$–145° and $PA_z \approx 302^\circ$ to 327°. Fig. 12 illustrates the orientation of η Car's binary orbit on the sky relative to the Homunculus. With $i \approx 138^\circ$, $\theta \approx 7^\circ$ and $PA_z \approx 317^\circ$, the resulting projected orbit on the sky has η_B moving *clockwise* relative to η_A, with η_B approaching η_A from the SW prior to periastron, and receding to the NE afterward.

In their recent work modelling η Car's *RXTE* light curve, O08 and P09 investigated values of i in the range $0^\circ < i < 90^\circ$, and each obtained a best-fitting value of $i \approx 42^\circ$, which they state is consistent with the orbital axis of the η Car binary being aligned with the Homunculus polar axis. However, the inclination angle of the Homunculus, as defined in Davidson et al. (2001) and Smith (2006), corresponds to the tilt of the polar axis out of the line of sight (fig. 5 of Davidson et al. 2001). Since this is the same quantity as the inclination defined for binary orbits, the polar axis of the Homunculus is tilted from the plane of the sky by ∼48°. Therefore, an $i \approx 138^\circ$ is required in order for the η Car orbital axis to be aligned with the Homunculus polar axis, *not* 42°.

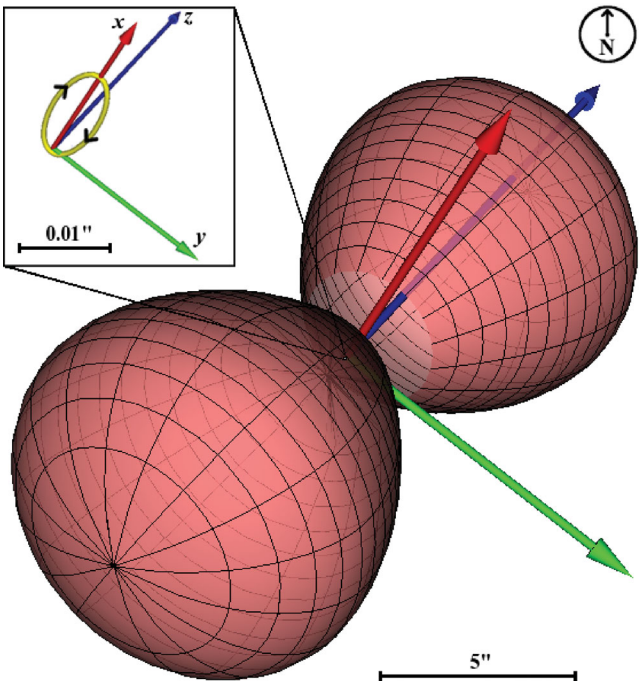

Figure 12. Illustration of η Car's binary orbit (inset, yellow) on the sky relative to the Homunculus nebula for a binary orientation with $i = 138^\circ$, $\theta = 7^\circ$ and $PA_z = 317^\circ$, which lies near the centre of our best-fitting range of orbital parameters. The $+z$ orbital axis (blue) is closely aligned with the Homunculus polar axis in 3D. η_B orbits clockwise on the sky relative to η_A (black arrows in inset), and apastron is on the observer's side of the system. The semimajor axis ($+x$-axis, red) runs from NW to SE on the sky, while the semiminor axis ($+y$-axis, green) runs from SW to NE. North is up.

The spatially unresolved nature of the X-ray observations and overall top–bottom symmetry of the problem are what allowed O08 and P09 to reasonably reproduce the *RXTE* light curve using an $i \approx 42^\circ$. However, an $i \approx 138^\circ$ works as well. Moreover, with either i, *any* PA on the sky of the orbital axis produces a good fit to the *RXTE* light curve. Unfortunately, this ambiguity in i and PA of the orbital axis has not been sufficiently discussed in the η Car literature, and most have simply assumed that the orbital and Homunculus polar axes are aligned. Yet, knowing the value of i is crucial for proper interpretation of spatially resolved observational diagnostics and, most importantly, determining the stellar masses.

Taking into account this ambiguity in i inherent to 3D models of X-ray data, our derived ranges of i and θ agree very well with those of O08, P09 and P11. They are also consistent with the i and ω values derived by Groh et al. (2010b) in their attempts to understand the origin of the high-velocity (up to $-1900\,km\,s^{-1}$) absorption wing detected in He I λ10830 during η Car's 2009 periastron passage. Our binary orientation is in complete agreement with simple models proposed to explain the available radio (Duncan & White 2003; White et al. 2005) and He II λ4686 (Teodoro et al. 2011) observations as well.

Further support for our results and derived orbital orientation comes from recent work by Mehner et al. (2010), who mapped the flux of the broad, blueshifted component of [Fe III] λ4659 and found that most of the emission originates in the inner 0.15 arcsec region of η Car (see their fig. 8). The synthetic spectroimages and 2D spatial maps of [Fe III] λ4659 in Section 4 show that most of the emission should indeed originate in the inner 0.15 arcsec. According to our 3D model, this emission forms in/near the current WWC zone in regions photoionized by η_B and manifests itself in spectroimages as a bright, central streak in the inner ±0.15 arcsec that spans a wide range of velocities from blue to red. This emission appears as a bright central streak because *HST*/STIS lacks the resolution necessary to resolve the inner WWC region's complex features.

Mehner et al. (2010) additionally found that the spatial distribution of the blueshifted component of [Fe III] λ4659 in the central 0.1 arcsec of η Car is not as sharp as a stellar point source and is detectably elongated to the NE and SW (see their figs 8 and 9). Model images displaying the 2D spatial distribution on the sky of the blueshifted component of [Fe III] λ4659 (first column of Figs 7, 10 and 11) show that the emission *is* elongated to the NE and SW for our suggested orbital orientation, even in the central 0.1 arcsec. While detailed mapping with *HST*/STIS is needed to verify the results of Mehner et al. (2010), they do strongly suggest that our 3D model and binary orientation are correct.

All other orbital orientations, such as that with $\theta \approx 180^\circ$ favoured by Falceta-Gonçalves et al. (2005), Abraham et al. (2005), Abraham & Falceta-Gonçalves (2007), Kashi & Soker (2007, 2008, 2009) and Falceta-Gonçalves & Abraham (2009), produce spectroimages that are in strong disagreement with the $\phi = 0.976$, PA = 38° observations, lacking any spatially extended, blueshifted emission and containing significant amounts of extended, redshifted emission. With η_B the main source of photons capable of producing high-ionization forbidden line emission, there is no realistic situation with $\theta \approx 180^\circ$, for any i and PA_z, that can produce spectroimages like those observed since there will always be an extended redshifted

component. Hypothesizing some method to absorb or diminish the redshifted emission does not help since there would then be almost *no* spatially extended emission detected at slit PA = 38°.

There is no known source of ionizing photons in the η Car system that permits a $\theta \approx 180°$ orientation. Photons generated in the WWC region will not work simply because the WWC zone is on the opposite side of the system during most of the orbit and η_A's dense wind would easily absorb any such photons before they reach the periastron side. Even if some contrived process could produce significant amounts of spatially extended, blueshifted emission on the periastron side of the system, this would not result in a match to the observations as the spectroimages would then contain both red- *and* blueshifted extended emission. There would have to be some way to absorb or diminish the extended, optically thin redshifted emission while allowing the blueshifted emission component to reach the observer. The problem is that extended, redshifted emission is observed at other slit PAs, even for similar orbital phases. Therefore, the absorption/diminution would have to be restricted to very specific, extended regions on the sky, which seems unrealistic. Given all of these issues, as well as those concerning the observed phase dependence of the emission, an orientation that places apastron on our side of the system seems unavoidable.

5.1.1 Observational support from the Weigelt blobs

While a detailed review of η Car's spectral variability is beyond the scope of this paper, it now seems well established that observed, phase-dependent, narrow ($\lesssim$50 km s^{-1}) high-ionization forbidden emission lines form in Weigelt blobs B, C and D (Davidson et al. 1995; Zethson 2001; Damineli et al. 2008a,b; Mehner et al. 2010; Zethson et al. 2011). Illumination of the Weigelt blobs by η_B is required for the formation of these narrow lines, which are present during most of η Car's 5.5-yr orbit, and fade during periastron passage, gradually returning to their 'normal' strength a few months afterward (Verner et al. 2005; Mehner et al. 2010).

Our proposed orientation and direction for η Car's binary orbit are consistent with, and provide an explanation for, the time variability of the narrow-line emission features seen in the Weigelt blobs. Davidson et al. (1995, 1997) found that Weigelt blobs B, C and D are located within 0.15 to 0.3 arcsec NW of the central stellar source near the Homunculus equatorial plane (see Fig. 2). Based on proper motions and observed blueshifted emission, the Weigelt blobs are located on the same side of η Car as the observer and are thought to have been ejected sometime around the smaller eruption of 1890 that also formed the Little Homunculus (Davidson & Humphreys 1997; Zethson 2001; Ishibashi et al. 2003; Smith et al. 2004; Nielsen, Ivarsson & Gull 2007a; Mehner et al. 2010). Since the Weigelt blobs are on the same side of the system as the observer, and because η_B is required for the formation of the narrow, high-ionization forbidden lines that form in the blobs during most of the orbit, one easily concludes that η_B must be on the same side of the system as the observer during most of the orbit.

Moreover, the Weigelt blobs are located in the NW quadrant of the system. For our proposed orbital orientation, during most of the orbit, the low-density wind cavity created by η_B is open toward and pointing NW, in the direction of the blobs. The low-density cavity thus provides a path for the ionizing photons from η_B to reach the Weigelt blobs and produce the high-ionization emission. Over the course of the 5.5-yr orbit, η_B gradually moves from SE to NW on the sky when going from periastron to apastron, and then from the NW back to the SE when moving from apastron to periastron. The orbital motion of η_B and gradual embedding in the wind of η_A close to periastron leads to changes in the spatial extent and direction of the photoionization region, which causes observed variations in the narrow, high-excitation emission in the blobs. During periastron passage, the ionizing flux from η_B shuts off, and the high-excitation emission from the blobs fades. It takes several months after periastron for η_B to restore the large photoionization volume that faces NW, and thus the high-excitation emission in the blobs.

While omitting some of the details, this qualitative picture is consistent with the known behaviour of the Weigelt blobs. The proposed clockwise direction of η_B's orbit is further supported by the images of Smith et al. (2004), which show excess UV emission to the SW of η Car just before periastron, and to the NE just after. A complete review of all of the available observations of η Car and how they support the derived orientation and direction of the binary orbit is obviously not possible here. However, we note that the orientation shown in Fig. 12 and clockwise motion on the sky of η_B are consistent with all known observations of η Car to date.

5.2 Implications for theories for the formation of the Homunculus nebula and the nature of η_A's wind

A variety of models, ranging from the interaction of stellar winds with differing speeds and densities, to binary interactions and even a binary merger, have been proposed for explaining both the Great Eruption and the bipolar shape of the resulting nebula (Smith 2009). Observational studies of the Homunculus have firmly established that its polar axis is orientated on the sky at a PA $\simeq$ 312°, and that its inclination is 42° ± 1° (Davidson et al. 2001; Smith 2006, 2009). As shown in Fig. 12, the orbital axis of the η Car binary for our best-fitting range of orientation parameters is closely aligned in 3D with the Homunculus polar axis. Such an alignment has important implications for theories for the formation of the Homunculus and/or the present-day shape of η_A's wind.

HST/STIS long-slit spectral observations of the Homunculus by Smith et al. (2003) indicate that the reflected stellar spectrum over the poles has stronger and broader absorption in Hα, implying a denser, polar outflow. Very Large Telescope (VLT)/Very Large Telescope Interferometer (VLTI) observations of the optically thick stellar wind of η_A by van Boekel et al. (2003) and Weigelt et al. (2007) also indicate that η_A's wind could be prolate in shape and aligned at the same PA on the sky as the Homunculus. Many have interpreted these observational studies as evidence for the current-day wind of η_A being prolate, with a bipolar form and orientation similar to the Homunculus. Thus, one explanation offered for both the Homunculus' formation and the nature of the present-day wind is that η_A is a rapid rotator (Owocki & Gayley 1997; Maeder & Meynet 2000; Dwarkadas & Owocki 2002; Smith et al. 2003; Owocki, Gayley & Shaviv 2004); the effects of gravity darkening on radiation-driven wind outflows from a rapidly rotating star suggested as a way of explaining both the high polar densities and velocities inferred in η_A's extended wind.

However, using 2D radiative transfer models, Groh et al. (2010a) and Groh (2011) find that the density structure of η_A's wind can be sufficiently disturbed by η_B, thus strongly affecting the observed UV spectrum, optical hydrogen lines and mimicking the effects of fast rotation in the interferometric observables. Groh et al. (2010a) further show that even if η_A is a fast rotator, models of the interferometric data are not unique, and both prolate- and oblate-wind models can reproduce the interferometric observations. These prolate- and oblate-wind models additionally suggest that the rotation axis of η_A would not be aligned with the Homunculus polar axis. Further

complicating the situation are the recent results of Mehner et al. (2011), who find no evidence for higher wind velocities at high stellar latitudes in Hδ P Cygni profiles obtained during η Car's normal state (see their Section 5). Together, these new results challenge the idea that the present-day wind of η_A is latitudinally dependent and prolate in shape.

In this context, it is noteworthy that the results in Section 4 match the observations so well, given that the winds from both stars are assumed to be spherical in the 3D simulations. New 3D simulations with a latitudinal-dependent wind for η_A, and comparison of the resulting spectroimages to the observations, may provide additional clues as to the nature of η_A's present-day wind. It is important to keep in mind though that these new results do not necessarily mean that η_A's wind was not latitudinally dependent in the past. Latitudinal-dependent mass loss from a rapidly rotating η_A could have played a role in the formation of the Homunculus. However, the argument for this possibility should not be made based on the above-mentioned observations of η_A's current-day wind.

If η_A's rotation axis is aligned with the orbital axis, and the star is a rapid rotator, then the extended wind should be prolate and aligned at nearly the same PA as the Homunculus. However, the orbital axis and rotation axis of η_A do not have to be aligned. This is another common assumption, with important implications for theories proposed to explain η Car's spectroscopic events (Davidson & Humphreys 1997; Smith et al. 2003; Mehner et al. 2011). Future observations using diagnostics that are not significantly affected by η_B are needed to determine whether or not η_A is a rapid rotator, and whether its rotation axis is aligned with the orbital axis.

Alignment of the orbital and Homunculus polar axes strongly suggests that binarity played a role in the Great Eruption, and possibly the smaller eruption that later formed the Little Homunculus. A binary merger seems unlikely given the multiple known large eruptions of the system (Smith 2009). The most likely situation involves some sort of interaction between η_A and η_B at periastron. Smith et al. (2003) suggested a scenario in which a rotating η_A loses mass due to increased angular momentum caused by an interaction with η_B. Models for the periastron-passage triggering of η Car's massive eruptions, and the requirement of a binary to explain the bipolar shape of the Homunculus, have also been proposed by Soker and colleagues (Soker 2004, 2007; Kashi & Soker 2010).

More recently, Smith & Frew (2011) presented a revised historical light curve for η Car, showing that two 100-d peaks observed in 1838 and 1843 just before the Great Eruption coincide to within weeks of periastron, provided the orbital period then was shorter than the current period by $\sim$5 per cent. The beginning of η Car's lesser outburst in 1890 also seems to have occurred around periastron (Smith & Frew 2011). Based on these findings and other considerations, Smith (2011) proposes that a stellar collision occurred at periastron before and during η Car's Great Eruption, with η_B plunging deeply into the bloated photosphere of η_A. Is close alignment of the orbital axis and polar axis of the Homunculus evidence for such a scenario? Only detailed theoretical modelling can answer this question, but given the now apparent alignment of the two axes, binary interaction scenarios should be seriously considered as possible explanations for η Car's multiple, massive eruptions.

5.3 Probing changes in η Car's stellar and wind parameters via long-term monitoring of the forbidden line emission

The η Car system not only has a centuries-long history of variation, including two major eruptions, it exhibits shorter term variability with a 5.5-yr period (Davidson & Humphreys 1997; Humphreys, Davidson & Koppelman 2008; Smith & Frew 2011). This implies that η Car's numerous spectroscopic events are also related to periastron passage (Damineli et al. 2008a,b). Contrary to many expectations, η Car's 2009.0 spectroscopic event was considerably different than that of earlier cycles (C11; Mehner et al. 2011). The observed X-ray minimum in 2009 was substantially shorter than the minima in 1998 and 2003, by approximately one month (C10, C11). The emission strength of Hα and various X-ray lines also appears to have decreased by factors of order 2 (C11). Recent *HST* WFPC2 observations by Mehner et al. (2011) show that the minimum in the UV was much deeper (again by about a factor of 2) for the 2009 event than for the 2003 event. While still the subject of debate, the behaviour of [He II] λ4686 might have been different in 2009 as well, with a second 'outburst' occurring $\sim$30 d after the first (Mehner et al. 2011; Teodoro et al. 2011).

The cause of this sudden change in the behaviour of η Car's spectroscopic event is still poorly understood. One proposed explanation is that the mass-loss rate of η_A has suddenly decreased by at least a factor of 2 (C10, C11; Mehner et al. 2011). However, this is far from confirmed and the exact reasons for such a drop are unknown. The results in this paper suggest a possible way to observationally test the idea that η_A's mass-loss rate has recently changed. All of the *HST*/STIS observations modelled were taken in or before 2004. The model in this paper assumes a mass-loss rate of 10^{-3} M$_\odot$ yr^{-1} for η_A, which is based on earlier observational and modelling studies (Davidson & Humphreys 1997; H01, H06). The good match between the synthetic spectroimages and the observations suggests that the mass-loss rate of η_A was $\sim 10^{-3}$ M$_\odot$ yr^{-1} at the time the observations were taken.

The results in Section 4 though are strongly dependent on the mass-loss rate assumed for η_A and the ionizing flux of photons assumed for η_B. If the ionizing flux of photons from η_B remains constant, but the mass-loss rate of η_A drops by a factor of 2 or more, the size of the photoionization region should increase considerably. Therefore, the spatial extent and flux of the observed high-ionization forbidden lines should also drastically change. The phase dependence of the forbidden emission would likely differ, with the high-ionization emission vanishing at later phases (compared to earlier orbital cycles) when going into periastron, and reappearing at earlier phases afterward. Observed variations with slit PA should be different too, possibly showing longer spatially extended structures, and even new components at different v_{los}. Changes in the wind terminal velocity of η_A could be similarly investigated using the maximum observed v_{los} of the spatially extended emission.

Multi-epoch observations coupled with improved 3D radiative transfer modelling of the high-ionization forbidden line emission would also help in determining if there is a significant change in η_B's ionizing flux of photons, mass-loss rate or wind terminal speed. Constraints on the ionizing flux of photons from η_B could be compared to stellar models for a range of O (Martins et al. 2005) and WR (Crowther 2007) stars, allowing one to obtain a luminosity and temperature for η_B.

6 SUMMARY AND CONCLUSIONS

A major goal of this paper has been to use the 3D dynamical model and available *HST*/STIS observations of high-ionization forbidden lines to constrain the absolute 3D orientation and direction of η Car's binary orbit. The spatially resolved spectroscopic observations obtained with the *HST*/STIS provide the crucial spatial *and* velocity information needed to help accomplish this. Since the forbidden

lines do not have an absorption component, they provide a clear view throughout η Car's extended interacting winds. Each high-ionization forbidden line arises *only* in regions where (1) photoionization by η_B can produce the required ion, (2) the density is near the line's critical density and (3) the material is at the appropriate temperature. Our results are therefore not as dependent on the many complicated details and effects encountered when modelling other forms of emission and/or absorption, such as X-rays or spectral features of H I, He I or other species (H01, H06; Nielsen et al. 2007b; P11).

Synthetic spectroimages of [Fe III] emission-line structures generated using 3D SPH simulations of η Car's binary WWC and radiative transfer codes were compared to the available *HST*/STIS observations for a variety of orbital phases and STIS slit PAs. The model spectroimages provide important details about the physical mechanisms responsible for the observed high-ionization forbidden line emission, as well as the location and orientation of the observed emitting structures. Below, we summarize our key conclusions and outline the direction of future work.

(i) Large-scale ($\sim$1600 au) 3D SPH simulations of η Car's binary colliding winds show that during periastron passage, the dense wind of η_A flows unimpeded in the direction of system apastron (Fig. 6). Following periastron, η_B's high-velocity wind collides with this primary wind material, creating dense shells that expand outward during η Car's 5.5-yr orbital cycle. These shells eventually fragment, forming a pair of dense, spatially extended 'arcs' of primary wind on the apastron side of the system. After several orbital cycles, the arcs drop in density and mix with the surrounding low-density wind material from η_B.

(ii) During most of η Car's orbit, far-UV radiation from η_B photoionizes a significant, spatially extended region on the apastron side of the system, including portions of the dense arcs of primary wind formed following periastron (Fig. 6). Portions of the current WWC region and primary wind just beyond it are also photoionized by η_B. The density and temperature of the material in these regions are ideal for producing [Fe III] emission (Fig. 6).

(iii) During periastron passage, η_B becomes enveloped in the dense wind of η_A. This significantly reduces the size of the photoionization region, to approximately a few semimajor axes in diameter. Since the large photoionization region has 'collapsed', the spatially extended (>0.1 arcsec) high-ionization forbidden line emission vanishes during periastron passage ($\phi \approx 0.99$–1.07). It does not reappear until η_B completes periastron passage and restores the extended photoionization region, which can take several months.

(iv) Synthetic spectroimages of [Fe III] λ4659 show that most of the [Fe III] emission originates in the central 0.15 arcsec, in agreement with fig. 8 of Mehner et al. (2010). Our 3D model shows that this emission forms in photoionized material near the current WWC zone, which is not spatially resolved by *HST*/STIS. Spatially extended (>0.15 arcsec) [Fe III] emission arises in photoionized portions of the expanding arcs of primary wind formed just after periastron passage.

(v) Only spectroimages generated for lines-of-sight angled $\theta = -15^\circ$ to $+30^\circ$ prograde of the semimajor axis on the apastron side of the system are able to match the observations taken at $\phi = 0.976$, slit PA $= 38^\circ$. However, there is an ambiguity in the orbital inclination i, with models for $i = 35^\circ$ to 50°, PA$_z = 272^\circ$ to 332° and $i = 130^\circ$ to 145°, PA$_z = 282^\circ$ to 342° both able to produce entirely blueshifted arcs (Fig. 7).

(vi) Model spectroimages of multiphase observations obtained at slit PA $= -28^\circ$ break the above degeneracy in i, fully constraining η Car's orbital orientation parameters. Given the uncertainties in some of the stellar/wind parameters used in the 3D modelling, *our suggested best-fitting range of orientation parameters for the η Car binary system are* $i \approx 130^\circ$ to 145°, $\theta \approx -15^\circ$ to $+30^\circ$, PA$_z \approx 302^\circ$ to 327°. Therefore, *the orbital axis of the η Car binary system is closely aligned in 3D with the Homunculus polar axis, with apastron on the observer's side of the system and η_B orbiting clockwise on the sky relative to η_A* (Fig. 12).

(vii) All other orbital orientations, including that in which η_B is in front of η_A at periastron ($\theta = 180^\circ$), are explicitly ruled out as they produce model spectroimages that lack entirely blueshifted, spatially extended arcs, containing instead significant amounts of unobserved, spatially extended redshifted emission at $\phi = 0.976$, slit PA $= 38^\circ$ (Fig. 8).

(viii) The 3D model predicts that the orientation on the sky of the blueshifted component of [Fe III] λ4659 should not vary much during η Car's orbit, stretching from NE to SW. However, the spatial extent of the emission should grow larger as the system moves from periastron to apastron, and decrease in size close to periastron. The orientation and spatial extent of the redshifted component should behave in a way similar to that of the blueshifted component, but pointing NW on the sky.

(ix) The apparent alignment of the orbital axis and Homunculus polar axis implies a link between binarity and η Car's numerous massive eruptions. Binary interaction scenarios should be seriously considered as possible explanations for the Great Eruption and formation of the bipolar Homunculus, and possibly the smaller eruption in 1890 that formed the Little Homunculus.

(x) Future detailed 3D simulations and radiative transfer calculations, together with high-resolution spatial mapping of the high-ionization forbidden line emission with *HST*/STIS, have the potential to further constrain the temperature and luminosity of η_B. The strong dependence of the forbidden line emission on the mass-loss rate of η_A and ionizing flux of photons from η_B may provide clues as to the nature of η Car's long-term variability, specifically, the cycle-to-cycle variations of the spectroscopic events.

The 3D dynamical modelling in this paper and the available *HST*/STIS spectral observations have increased our understanding of the η Car system. Much work remains, however. Efforts are underway to improve both the 3D hydrodynamical modelling and 3D radiative transfer approach. New 3D simulations that include radiative cooling, radiation-driven stellar winds, gravity and effects like radiative inhibition and braking are on the horizon. Preliminary results of detailed 3D radiative transfer calculations using SimpleX (Paardekooper 2010) are promising as well. With these new tools at our disposal, it should be possible to further constrain the stellar, wind, and orbital parameters of η Car, setting the stage for orbital modelling to determine the stellar masses.

ACKNOWLEDGMENTS

TIM and CMPR were supported through the NASA Graduate Student Researchers Program. TIM and JHG also thank the Max Planck Society for financial support for this work. All SPH simulations were performed on NASA Advanced Supercomputing (NAS) facilities using NASA High End Computing (HEC) time. SPO acknowledges partial support from NASA ATP grant NNK11AC40G. TRG

acknowledges the hospitality of the MPIfR during the completion of this paper.

REFERENCES

Abdo A. A. et al., 2010, ApJ, 723, 649
Abraham Z., Damineli A., 1999, in Morse J. A., Humphreys R. M., Damineli A., eds, ASP Conf. Ser. Vol. 179, Eta Carinae at The Millennium. Astron. Soc. Pac., San Francisco, p. 263
Abraham Z., Falceta-Gonçalves D., 2007, MNRAS, 378, 309
Abraham Z., Falceta-Gonçalves D., Dominici T., Caproni A., Jatenco-Pereira V., 2005, MNRAS, 364, 922
Bryans P., Badnell N. R., Gorczyca T. W., Laming J. M., Mitthumsiri W., Savin D. W., 2006, ApJS, 167, 343
Corcoran M. F., 2005, AJ, 129, 2018
Corcoran M. F., 2011, Bull. Soc. R. Sci. Liege, 80, 578 (C11)
Corcoran M. F., Hamaguchi K., Pittard J. M., Russell C. M. P., Owocki S. P., Parkin E. R., Okazaki A., 2010, ApJ, 725, 1528 (C10)
Cox P., Mezger P. G., Sievers A., Najarro F., Bronfman L., Kreysa E., Haslam G., 1995, A&A, 297, 168
Crowther P. A., 2007, ARA&A, 45, 177
Damineli A., 1996, ApJ, 460, L49
Damineli A., Kaufer A., Wolf B., Stahl O., Lopes D. F., de Araújo F. X., 2000, ApJ, 528, L101
Damineli A. et al., 2008a, MNRAS, 384, 1649
Damineli A. et al., 2008b, MNRAS, 386, 2330
Davidson K., 1999, in Morse J. A., Humphreys R. M., Damineli A., eds, ASP Conf. Ser. Vol. 179, Eta Carinae at The Millennium. Astron. Soc. Pac., San Francisco, p. 304
Davidson K., 2005, in Humphreys R., Stanek K., eds, ASP Conf. Ser. Vol. 332, The Fate of the Most Massive Stars. Astron. Soc. Pac., San Francisco, p. 101
Davidson K., Humphreys R. M., 1997, ARA&A, 35, 1
Davidson K., Ebbets D., Weigelt G., Humphreys R. M., Hajian A. R., Walborn N. R., Rosa M., 1995, AJ, 109, 1784
Davidson K. et al., 1997, AJ, 113, 335
Davidson K., Ishibashi K., Gull T. R., Humphreys R. M., 1999, in Morse J. A., Humphreys R. M., Damineli A., eds, ASP Conf. Ser. Vol. 179, Eta Carinae at The Millennium. Astron. Soc. Pac., San Francisco, p. 227
Davidson K., Smith N., Gull T. R., Ishibashi K., Hillier D. J., 2001, AJ, 121, 1569
Dopita M. A., Sutherland R. S., 2003, Diffuse Matter in the Universe. Springer-Verlag, Heidelberg
Duncan R. A., White S. M., 2003, MNRAS, 338, 425
Dwarkadas V., Owocki S. P., 2002, ApJ, 581, 1337
Falceta-Gonçalves D., Abraham Z., 2009, MNRAS, 399, 1441
Falceta-Gonçalves D., Jatenco-Pereira V., Abraham Z., 2005, MNRAS, 357, 895
Feast M., Whitelock P., Marang F., 2001, MNRAS, 322, 741
Fernández-Lajús E. et al., 2010, New Astron., 15, 108
Groh J., 2011, Bull. Soc. R. Sci. Liege, 80, 590
Groh J. H., Madura T. I., Owocki S. P., Hillier D. J., Weigelt G., 2010a, ApJ, 716, L223
Groh J. H. et al., 2010b, A&A, 517, A9
Gull T. R. et al., 2009, MNRAS, 396, 1308 (G09)
Hamaguchi K. et al., 2007, ApJ, 663, 522
Hartman H., 2003, PhD dissertation, Lund Observatory, Lund University, Sweden
Henley D. B., 2005, PhD dissertation, Univ. Birmingham
Henley D. B., Corcoran M. F., Pittard J. M., Stevens I. R., Hamaguchi K., Gull T. R., 2008, ApJ, 680, 705
Hillier D. J., 1988, ApJ, 327, 822
Hillier D. J., Allen D. A., 1992, A&A, 262, 153
Hillier D. J., Davidson K., Ishibashi K., Gull T., 2001, ApJ, 553, 837 (H01)
Hillier D. J. et al., 2006, ApJ, 642, 1098 (H06)
Humphreys R. M., Davidson K., Koppelman M., 2008, AJ, 135, 1249
Iben I., Jr, 1999, in Morse J. A., Humphreys R. M., Damineli A., eds, ASP Conf. Ser. Vol. 179, Eta Carinae at The Millennium. Astron. Soc. Pac., San Francisco, p. 367
Ignace R., Brimeyer A., 2006, MNRAS, 371, 343
Ignace R., Bessey R., Price C. S., 2009, MNRAS, 395, 962
Ishibashi K., Corcoran M. F., Davidson K., Swank J. H., Petre R., Drake S. A., Damineli A., White S., 1999, ApJ, 524, 983
Ishibashi K. et al., 2003, AJ, 125, 3222
Kashi A., Soker N., 2007, New Astron., 12, 590
Kashi A., Soker N., 2008, MNRAS, 390, 1751
Kashi A., Soker N., 2009, MNRAS, 397, 1426
Kashi A., Soker N., 2010, ApJ, 723, 602
Krist J., Hook R., 1999, The Tiny Tim User's Guide. STScI, Baltimore
Madura T. I., 2010, PhD dissertation, Univ. Delaware
Maeder A., Meynet G., 2000, ARA&A, 38, 143
Martins F., Schaerer D., Hillier D. J., 2005, A&A, 436, 1049
Mehner A., Davidson K., Ferland G. J., Humphreys R. M., 2010, ApJ, 710, 729
Mehner A., Davidson K., Martin J. C., Humphreys R. M., Ishibashi K., Ferland G. J., 2011, ApJ, 740, 80
Mihalas D., 1978, Stellar Atmospheres. Freeman & Co., New York
Monaghan J. J., 2005, Rep. Progress Phys., 68, 1703
Nahar S. N., 1997, Phys. Rev. A, 55, 1980
Nahar S. N., Pradhan A. K., 1996, A&AS, 119, 509
Nielsen K. E., Ivarsson S., Gull T. R., 2007a, ApJS, 168, 289
Nielsen K. E., Corcoran M. F., Gull T. R., Hillier D. J., Hamaguchi K., Ivarsson S., Lindler D. J., 2007b, ApJ, 660, 669
Nussbaumer H., Vogel M., 1987, A&A, 182, 51
Okazaki A. T., Owocki S. P., Russell C. M. P., Corcoran M. F., 2008, MNRAS, 388, L39 (O08)
Osterbrock D. E., 1989, Astrophysics of Gaseous Nebulae and Active Galactic Nuclei. University Science Books, Mill Valley, CA
Owocki S. P., Gayley K. G., 1997, in Nota A., Lamers H., eds, ASP Conf. Ser. Vol. 120, Luminous Blue Variables: Massive Stars in Transition. Astron. Soc. Pac., San Francisco, p. 121
Owocki S. P., Gayley K. G., Shaviv N. J., 2004, ApJ, 616, 525
Paardekooper J.-P., 2010, PhD dissertation, Leiden Observatory, Leiden University, Netherlands
Parkin E. R., Pittard J. M., Corcoran M. F., Hamaguchi K., Stevens I. R., 2009, MNRAS, 394, 1758 (P09)
Parkin E. R., Pittard J. M., Corcoran M. F., Hamaguchi K., 2011, ApJ, 726, 105 (P11)
Pittard J. M., 1998, MNRAS, 300, 479
Pittard J. M., 2000, PhD dissertation, Univ. Birmingham
Pittard J. M., Corcoran M. F., 2002, A&A, 383, 636 (PC02)
Price D. J., 2004, PhD dissertation, Institute of Astronomy and Churchill College, Univ. Cambridge
Price D. J., 2007, Publ. Astron. Soc. Australia, 24, 159
Richardson N. D., Gies D. R., Henry T. J., Fernández-Lajús E., Okazaki A. T., 2010, AJ, 139, 1534
Smith N., 2006, ApJ, 644, 1151
Smith N., 2009, preprint (arXiv:0906.2204)
Smith N., 2011, MNRAS, 415, 2020
Smith N., Frew D. J., 2011, MNRAS, 415, 2009
Smith N., Owocki S., 2006, ApJ, 645, L45
Smith N., Davidson K., Gull T. R., Ishibashi K., Hillier D. J., 2003, ApJ, 586, 432
Smith N. et al., 2004, ApJ, 605, 405
Soker N., 2004, ApJ, 612, 1060
Soker N., 2007, ApJ, 661, 490
Tavani M. et al., 2009, ApJ, 698, L142
Teodoro M. et al., 2011, ApJ, preprint (arXiv:1104.2276)
van Boekel R. et al., 2003, A&A, 410, L37
van Genderen A. M., Sterken C., Allen W. H., Walker W. S. G., 2006, J. Astron. Data, 12, 3
Verner E., Bruhweiler F., Gull T., 2005, ApJ, 624, 973

Vishniac E. T., 1983, ApJ, 274, 152
Weigelt G., Ebersberger J., 1986, A&A, 163, L5
Weigelt G. et al., 2007, A&A, 464, 87
White S. M., Duncan R. A., Chapman J. M., Koribalski B., 2005, in Humphreys R., Stanek K., eds, ASP Conf. Ser. Vol. 332, The Fate of the Most Massive Stars. Astron. Soc. Pac., San Francisco, p. 126
Whitelock P. A., Feast M. W., Marang F., Breedt E., 2004, MNRAS, 352, 447
Williams P. M., 2008, Rev. Mex. Astron. Astrofis. Conf. Ser., 33, 71
Wünsch R., Dale J. E., Palous J., Whitworth A. P., 2010, MNRAS, 407, 1963
Zanella R., Wolf B., Stahl O., 1984, A&A, 137, 79
Zethson T., 2001, PhD dissertation, Lunds Universitet, Sweden
Zethson T., Johansson S., Hartman H., Gull T. R., 2011, A&A, submitted
Zhang H., 1996, A&AS, 119, 523

SUPPORTING INFORMATION

Additional Supporting Information may be found in the online version of this article:

Appendix A. Masking procedure for the *HST*/STIS observations.
Appendix B. Forbidden line emission theory.

Please note: Wiley-Blackwell are not responsible for the content or functionality of any supporting materials supplied by the authors. Any queries (other than missing material) should be directed to the corresponding author for the article.

This paper has been typeset from a TEX/LATEX file prepared by the author.